Key Points:
- Olivine-spinel transformation in laboratory experiments can cause deep-focus earthquakes analogs in both fine- and coarse-grained aggregates
- Transformational faulting follows the scaling laws of natural earthquakes, as evidenced by calibrated acoustic emissions experiments
- Structural heterogeneity in slabs affects the b-values of deep-focus earthquakes

Supporting Information:

Supporting Information may be found in the online version of this article.

Correspondence to:

S. Sawa,
sando-sawa@tohoku.ac.jp

Author Contributions:

Conceptualization: S. Sawa, J. Gasc, A. Schubnel, J. Muto
Data curation: S. Sawa
Formal analysis: N. Miyajima
Funding acquisition: S. Sawa, A. Schubnel, J. Muto
Investigation: S. Sawa
Methodology: S. Sawa, J. Gasc, N. Miyajima, A. Schubnel, M. Baïsset, J. Muto
Software: M. Baïsset
Supervision: J. Gasc, A. Schubnel, J. Muto
Visualization: N. Miyajima
Writing – original draft: S. Sawa
Writing – review & editing: J. Gasc, N. Miyajima, A. Schubnel, M. Baïsset, J. Muto

Magnitude Distribution During Transformational Faulting: Implication for Deep-Focus Earthquakes

S. Sawa[1] , **J. Gasc[2]** , **N. Miyajima[3]** , **A. Schubnel[2]** , **M. Baïsset[2]** , and **J. Muto[1]**

[1]Department of Earth Science, Graduate School of Science, Tohoku University, Sendai, Japan, [2]Laboratoire de Géologie, École Normale Supérieure, Paris, France, [3]Bayerisches Geoinstitut, University of Bayreuth, Bayreuth, Germany

Abstract Deep-focus earthquakes occur at 300–660 km depth. Geophysical observations and deformation experiments have proposed the olivine-spinel (wadsleyite/ringwoodite) phase transformation as the source of the mechanical instability. While geophysical observations indicate that fault geometry influences the b-values of the Gutenberg-Richter law for transformational faulting, deformation experiments reveal that b-values are also influenced by rock properties, including structural heterogeneity. Grain sizes play a crucial role in the rate of phase transformation, impacting the occurrence of faulting. Consequently, grain sizes may also influence b-values. We conducted deformation experiments on germanate olivine (Mg_2GeO_4), an analog to silicate olivine, with various grain sizes to reveal the effect of grain size on b-value during transformational faulting. We used a Griggs-type deformation apparatus and measured acoustic emissions (AE) with an AE transducer, which was calibrated by laser-doppler interferometry. This calibration enabled the acquisition of AE waveforms with a unit of velocity (m/s), facilitating comparison to natural earthquakes. b-values in the fine-grained aggregates (a few μm) are smaller than those in the coarse-grained aggregates (hundreds of μm) at the same deformation conditions. In coarse-grained aggregates, heterogeneous formation of spinel aggregates contributes to high b-values. Conversely, in fine-grained aggregates, homogeneous formation of spinel grains at the grain boundaries results in lower b-values. Therefore, the homogeneity (or heterogeneity) of spinel formation could be one of the factors controlling the b-values of deep-focus earthquakes.

Plain Language Summary Deep earthquakes, occurring between 300 and 660 km beneath the Earth's surface, are intriguing events. Geophysical observations and experiments point to mineral transformation from olivine to spinel phase as the key mechanism behind these deep earthquakes. Geophysical observations suggest that the shape of the fault influences the b-values of the Gutenberg-Richter law, which expresses the statistical distribution of moment magnitude and the number of earthquakes. However, experiments show that rock properties, such as its internal structure, may also play an important role. Grain size affects how fast olivine-spinel transformation occurs and, potentially, also influences the occurrence of earthquakes. In our deformation experiments using germanate olivine, a phase that is isostructural with silicate olivine, we varied grain-size and measured the absolute magnitudes of acoustic emission, laboratory proxies for natural earthquakes. Our findings reveal that b-values are smaller in fine-grained rocks than in coarse-grained rocks, as a result of homogeneous nucleation of spinel grains. Therefore, the homogeneity of phase transformation could control b-values. Understanding these processes provides valuable insights into the nature of deep earthquakes.

1. Introduction

Earthquakes occur as deep as 660 km below Earth's surface (e.g., Frohlich, 1989, 2006; Gutenberg & Richter, 1939; Wadati, 1928). Earthquakes at depths of 60–300 km and 300–660 km are called intermediate-depth earthquakes and deep-focus earthquakes, respectively (Frohlich, 2006). At high temperatures, rocks present ductile or semi-brittle behavior (e.g., Byerlee, 1968; Proctor & Hirth, 2016; Scholz, 1988, 1998; Shiraishi et al., 2022; Sibson, 1982; Simpson, 1985); therefore, a mechanism which must be different from that of shallow earthquakes is required to explain the occurrence of intermediate and deep-focus earthquakes.

Several mechanisms have been suggested: dehydration embrittlement (Hacker, Abers, & Peacock, 2003; Hacker, Peacock et al., 2003; Omori et al., 2004; Raleigh & Paterson, 1965; Zhang et al., 2021), thermal instability (Hobbs & Ord, 1988; John et al., 2009; Kanamori et al., 1998; Karato et al., 2001; Kikuchi & Kanamori, 1994; Ogawa, 1987), and transformational faulting (Burnley et al., 1991; Gasc, Daigre, et al., 2022,

Gasc, Gardonio, et al., 2022; Green & Burnley, 1989; Green et al., 1992; Incel et al., 2017; Riggs, 2005; Schubnel et al., 2013; Tingle et al., 1993; Wang et al., 2017). Geophysical observations suggest that deep-focus earthquakes are caused by a combination of transformational faulting and thermal instability (Wiens & McGuire, 1995; Zhan, 2017; Zhan et al., 2014) because only one mechanism by itself can not suffice in order to explain the diversity of deep-focus earthquakes (Jia et al., 2025; Suzuki & Yagi, 2011; Tibi et al., 2003; Wiens, 2001). In the transformational faulting mechanism (Green & Houston, 1995; Zhan, 2020), faulting occurs due to the phase transformation of one phase into another (e.g., from olivine to denser spinel phases: wadsleyite and ringwoodite). In the thermal instability model (Karato et al., 2001), when deformation occurs fast enough in comparison to the time scale of thermal diffusion, heat is accumulated in regions of high strain, creating a positive feedback between deformation and heating that results in thermal runaway. Zhan et al. (2014) and Zhan (2017) suggested that transformational faulting causes deep-focus earthquakes such as the 2013 Okhotsk earthquake with a magnitude M_w of 8.3 in a cold slab. Cold slabs contain a metastable olivine wedge of tens of kilometers thick, which is enough to host large deep-focus earthquakes caused by transformational faulting (Kawakatsu & Yoshioka, 2011; Zhan, 2017). Meanwhile, a combination of transformational faulting and thermal instability has been invoked to explain deep-focus earthquakes such as the 1994 Bolivia earthquakes with M_w 8.3 in a warm slab (Zhan et al., 2014). Warm slabs, in comparison to cold slabs, contain only a thin –if one at all– metastable olivine wedge. In such slabs, the rupture of deep-focus earthquakes can therefore initiate within metastable olivine wedge by transformational faulting, but can only further propagate outside the metastable olivine wedge by a different mechanism (Zhan, 2017). Zhan pointed out that the latter mechanism would be thermal instability, considering high energy dissipation (Kanamori et al., 1998). The possibility for such a dual mechanism, where rupture initiates via tranformational faulting in the metastable olivine and then propagates within spinel domains via frictional melting was recently confirmed by laboratory studies (Gasc, Daigre, et al., 2022). Furthermore, Zhan reported that the b-value of the Gutenberg-Richter law, $\log_{10}N = a - bM_w$ (N: number of earthquakes with magnitudes $\geq M_w$, a, b: constants), was close to 1 independent of magnitudes in cold slabs, whereas b was close to 0.5 for intermediate magnitudes (M_w 5.3 − 6.5) and increased to 1 for large magnitude ($M_w > 6.5$) in warm slabs. The author suggested that the difference in b-values for intermediate magnitudes (M_w 5.3 − 6.5) between warm and cold slabs is caused by the difference in the rupture geometry (Aki, 1981; Kanamori & Anderson, 1975). However, these estimations only provide average characteristics of deep-focus earthquakes. According to deformation experiments, the heterogeneity of rocks may also affect b-values (Mogi, 1962). However, the relationship between heterogeneous physical properties of rocks and seismic characteristics of deep-focus earthquakes remains unknown. In particular, grain size has a strong possibility of controlling b-values because it changes the rate of phase transformation, which in turn may affect the occurrence of faulting (Burnley et al., 1991; Cahn, 1956; Kubo et al., 1998, 2004).

In this study, we conducted deformation experiments on germanate olivine aggregates (an analog aggregate of silicate olivine) to determine the effect of grain size on b-values during transformational faulting. First, we conducted deformation experiments on aggregates of various grain sizes to reveal how phase transformation kinetics and characteristics change with grain size. Second, we conducted similar deformation experiments using an S wave transducer to detect acoustic emissions (AEs) during deformation. Finally, we calculated b-values for these experiments, and we relate the b-values dependency on the grain size of germanate aggregates and discuss the implications for structural heterogeneity in slabs.

2. Method

2.1. Sample Preparation

Samples were synthetic sintered germanate olivine-pyroxene aggregates (90 mol% Mg_2GeO_4 + 10 mol% $MgGeO_3$). Germanate olivine is an analog for silicate olivine (Vaughan & Coe, 1981), with which it is iso-structural, and has been widely used in deformation experiments aiming at reproducing deep-focus earthquakes in the laboratory (e.g., Burnley et al., 1991; Green & Burnley, 1989; Schubnel et al., 2013; Wang et al., 2017). Germanate powders were synthesized from MgO and GeO_2 powder mixtures according to Vaughan and Coe (1981), Shi et al. (2015), and Sawa et al. (2021). MgO and GeO_2 powders were mixed in a 2:1.05 molar ratio and homogenized by grinding in ethanol within an agate mortar. The powders were subsequently pressed into a cylindrical shape using stainless steel dies. The samples were then heated in air at 1,473 K for 96 hr, yielding
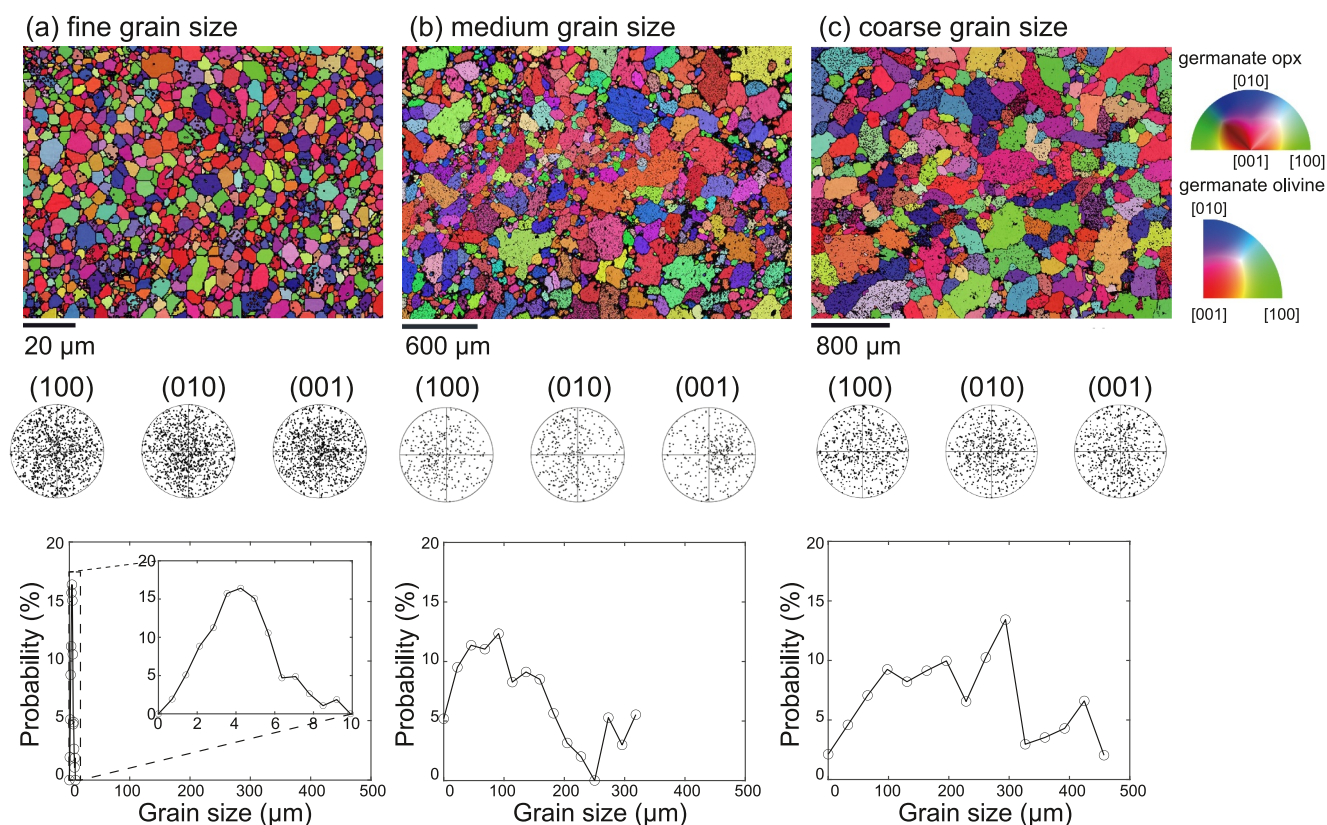
Figure 1. Inverse pole figure maps of germanate olivine and orthopyroxene, pole figures, and grain size distributions of germanate olivine in initial samples acquired by EBSD: (a) fine-grained aggregates (inset is the enlarged view), (b) medium-grained aggregates, and (c) coarse-grained aggregates.

germanate olivine-pyroxene aggregates powder after grinding. These germanate powders were then sintered at 1,413 K for 20 min using a spark plasma sintering method by SinterLand Inc. in Nigata, Japan to make fine-grained aggregates. The height and diameter of the sintered germanate aggregates (fine-grained aggregates) were approximately 15 and 30 mm, respectively. The average relative density was 95.6 ± 1.4%. Some of the sintered specimens were annealed in air at 1,723 K for 6 or 8 hr to make medium- and coarse-grained aggregates, respectively. Electron backscatter diffraction (EBSD, Oxford instruments) showed the absence of initial crystallographic preferred orientation (CPO) and allowed determination of mean grain sizes of fine-, medium- and coarse-grained aggregates of 4.3 μm, 135 μm, and 233 μm, respectively (shown in Figure 1).

2.2. Procedure of Deformation Experiments

Axial deformation experiments were conducted using a Griggs-type deformation apparatus. A schematic diagram of the entire assembly is illustrated in Figures 2a and 2b. A sample assembly utilizing NaCl as both outer and inner pressure media was used for the deformation experiments. After the target pressure and temperature conditions were reached, axial compression experiments were immediately performed at a constant strain rate. Initially, Pb, acting as a soft solid to seal the upper assembly portion between the sample and alumina pistons, was extruded along the deformation piston. Subsequently, the piston made contact with the sample top, accompanied by a abrupt increase in axial stress, known as the hit point (Holyoke & Kronenberg, 2010). All experiments were conducted within the stability field of germanate spinel (Ross & Navrotsky, 1987). However, germanate olivine retained a metastable state prior to axial compression due to the rapid heating rate (less than 1 hr) from 300° to the target temperature. Force and displacement data were converted to differential stress and strain, respectively, with corrections for the sample diameter changes and apparatus stiffness. The stress resolution of the Griggs-type apparatus is estimated to be 30–50 MPa (Hirth & Tullis, 1992; Kido et al., 2016). Experimental conditions are listed in Table 1.
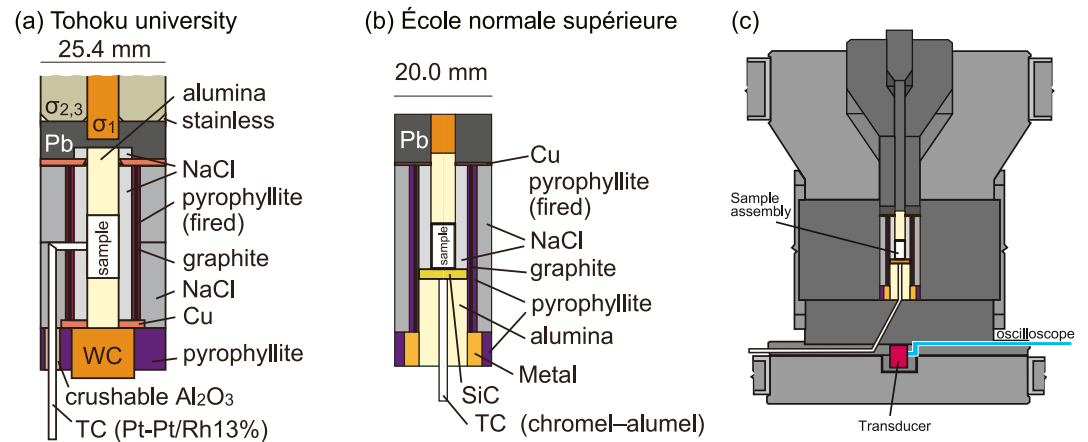
Figure 2. Schematic diagram of the whole sample assembly for the experiments (a) at Tohoku University and (b) at École Normale Supérieure. (c) Acoustic set-up modified after Moarefvand et al. (2021).

2.2.1. Axial Deformation Experiments at Tohoku University

Experiments GO143, GO144, GO145, GO147, and GO148 were conducted using the Griggs-type deformation apparatus installed at Tohoku University, Japan. The procedure of the deformation experiments was based on Kido et al. (2016) and Sawa et al. (2021). The construction of the assembly follows Post et al. (1996), Kido et al. (2016), Fukuda et al. (2018), and Sawa et al. (2021). Cylindrical samples with a height of 13 mm and a diameter of 6.25 mm were cored from the sintered specimens. The samples were enclosed within a Pt jacket using Pt discs at each end. They were subsequently inserted into an outer Ni jacket that slightly overlapped the end pistons.

The temperature was measured using an S-type thermocouple. Temperature and pressure were raised as follows: from room temperature to 100°C at 300 MPa, to 200°C at 550 MPa, and 300°C at 1,050 MPa. Then, pressure and temperature were elevated together to 1.2 GPa and to the target temperature, respectively. Axial compression was started immediately after with a constant strain rate of 1.0×10^{-4} s^{-1}. At the end of each experiment, the deformation was stopped, after which temperature was lowered to room temperature within 1 min.

Table 1
Experimental Conditions and Results

Run No.	P (GPa)	T (K)	$\dot{\varepsilon}$ (s^{-1})	Grain size	σ (GPa)	t (min)	Volume fraction of spinel	AE count	b-value
GO143	1.2	1173	1.0×10^{-4}	medium	1.45	98	24	–	–
GO144	1.2	1173	1.0×10^{-4}	coarse	1.59	71	9	–	–
GO145	1.2	1173	1.0×10^{-4}	fine	1.72	51	<1	–	–
GO147	1.2	973[1]	1.0×10^{-4}	coarse	1.87	54	0	–	–
GO148	1.2	1073	1.0×10^{-4}	fine	2.06	68	0	–	–
G116	1.5	1148	1.7×10^{-4}	fine	1.89	52	10	944	0.63 ± 0.04
G117	1.5	1148	1.0×10^{-4}	coarse	1.76	39	12	5,092	1.20 ± 0.03
G118	1.5	1265	1.5×10^{-4}	fine	0.46	34	22	258	1.16 ± 0.14
G120	1.5	1265	1.6×10^{-4}	coarse	0.34	42	21	21	4.11 ± 2.00
G123	1.5	1202	4.2×10^{-5}	coarse	0.43	168	28	20	–

Note. P: confining pressure, T: temperature, $\dot{\varepsilon}$: strain rate, σ: peak differential stress, and t: duration under high temperature (T). 1: This temperature was estimated from the power-temperature relations of previous experiments because of thermocouple failure.

2.2.2. Axial Deformation Experiments at École Normale Supérieure (ENS)

Experiments G116, G117, G118, G120, and G123 were conducted using the Griggs-type deformation apparatus installed at the École Normale Supérieure de Paris (ENS), France. These experiments were conducted with an S wave transducer to detect AEs during deformation. The procedure of the deformation experiments was based on Moarefvand et al. (2021). Cylindrical samples with a height of 8.9 mm and a diameter of 4.4 mm were cored from the sintered specimens. The samples were enclosed within a Pt jacket using Pt discs at each end. Temperature was measured below the sample capsule using a K-type thermocouple. This measurement was used to numerically estimate the temperature inside the sample by solving the heat equation according to Moarefvand et al. (2021). Detailed procedures and calculated results are available in Text S1 and Figure S2 in Supporting Information S1, respectively. The calculated thermal gradients are similar to those observed by Kirby and Kronenberg (1984). Pressure and temperature were elevated together up to the targeted conditions within 2h, and axial compression was performed immediately after at a constant strain rate. At the end of each experiment, the deformation piston was stopped and temperature was decreased to 873 K within 10 min. The experimental conditions are listed in Table 1.

2.3. AE Setting

An ultrasonic transducer (Olympus V156, 5 MHz center frequency), which exhibits primary sensitivity to S waves while maintaining capability to detect P waves, was used for experiments on G116, G117, G118, G120, and G123. The transducer was glued on an alumina ceramic disk with a high temperature 2-component epoxy, then directly glued on the back of the WC base plate (Figure 2c; Moarefvand et al., 2021). The acoustic signals were amplified and recorded both at 30 and 60 dB using a high-frequency amplifier. Data recording was only triggered when the acoustic signal rose above a certain threshold. 8,192-point acoustic waveform data were recorded at a sampling frequency of 50 MHz.

Because of the progressive degradation of the glue under cyclic temperature loading, the sensitivity of the transducer tends to decrease from one experiment to the next. We calibrated the sensitivity of the transducer at room conditions before each experiment by recording several AE generated on the WC baseplate. We calculated the average of the root mean square (RMS) of the recorded waveforms and used these averaged RMS values to normalize the moment magnitudes of the AEs acquired during each experiment so that they can be compared without bias from the decaying sensitivity of the transducer. The sensitivities of the S wave transducer S_t, relative to that of experiment G116 (i.e., which has a sensitivity of 1), were, in each of the following experiment (G117, 118, 120, 123), 0.813, 0.768, 0.693, and 0.181. The particularly low sensitivity of 0.181 in experiment G123 caused by the reduced bonding strength of the adhesive between the WC baseplate and transducer prevents us from using its results in our discussion. We used acoustic signals amplified to 60 dB but also used acoustic signals amplified to 30 dB when amplitudes of the signals amplified to 60 dB were saturated. To compare acoustic signals quantitatively, the amplitudes were all corrected to 0 dB.

P-wave and S-wave arrival times were picked manually (Figure S3 in Supporting Information S1). We could then calculate S-P travel time differences, $\Delta t = t_s - t_p$ (Gasc, Gardonio, et al., 2022), which, for AEs occurring at the bottom of sample are ∼3.5 μs. The travel time difference, Δt, between the top and bottom of the sample is ∼1 μs at room temperature using the P-wave velocity of germanate olivine. Therefore, δt for AEs occurring at the top of samples is ∼4.5 μs. For the following analysis, we used the acoustic signals with $\Delta t = 3.5 \sim 4.5$ μs, which corresponds to a one-dimensional location of the AE within the sample. The uncertainty of hypocenter locations depends on the volume fraction of transformed spinel and the accuracy of S-P intervals. An error of 0.1 μs in the S-P interval leads to an error of ∼1 mm in the hypocenter location.

Acoustic emission waveforms were initially acquired in Volts. The calibration procedure of Yoshimitsu et al. (2014) and Marty et al. (2023) was followed in order to transform the signal in units of velocity (m/s), then displacement upon signal intergration, so that common seismological parameters such magnitude, stress drop and corner frequency could be estimated.

The sensitivity function of the transducer $S_c(f)$ was obtained by combining a laser-doppler interferometry (Figure 3) and an acoustic source, for which a second transducer was glued on top of the WC base plate. A step voltage pulse was sent to the acoustic source, creating a ballistic wave for which surface vibrations were measured at the same location both by the acoustic emission transducer and the laser velocimeter. The sensitivity function of
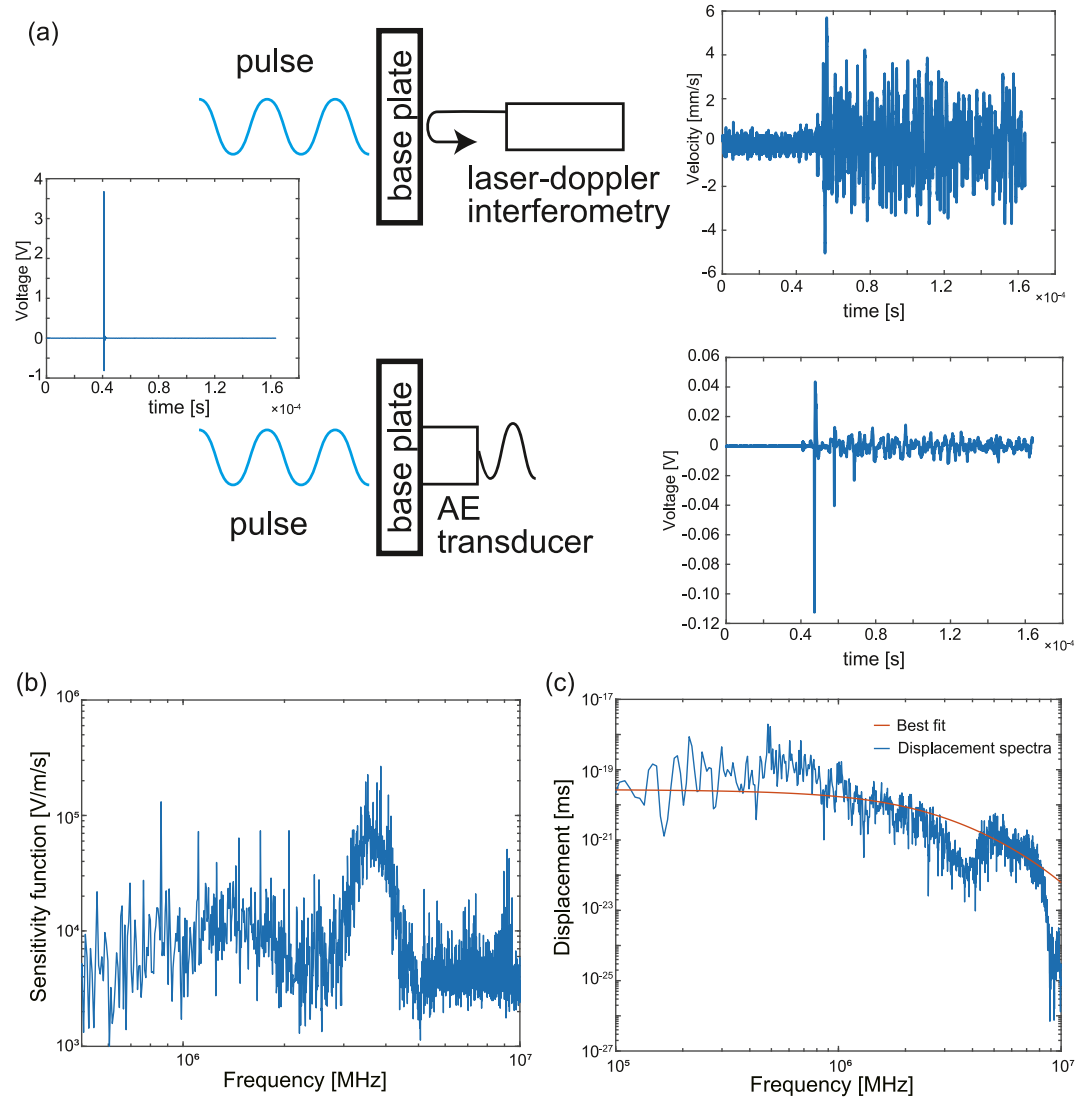
Figure 3. (a) Schematic of the setup used to calibrate the acoustic emissions (AE) transducer. (b) Sensitivity function of the AE transducer obtained from the waveforms measured by the AE transducer and recorded by laser-doppler interferometry. (c) Example of displacement spectrum fitting of an acoustic emission.

the AE transducer $S_c(f)$ was obtained in the frequency (f) domain by the deconvolution of the waveform measured by the AE transducer $I_a(f)$ out of the waveform recorded by the interferometry $I_l(f)$:

$$S_c(f) = \frac{I_a(f)}{I_l(f)}. \tag{1}$$

We obtained sensitivity functions (Figure 3b) for various input source voltages (50, 100, 150, 200, and 250 V) and durations (0.4, 0.2, 0.1 µs, corresponding to 2.5, 5.0, 10.0 MHz, respectively) applied to the broadband transducer. As observed by Marty et al. (2023), no significant difference was observed with respect to the amplitude and duration of input voltage. We then calculated an averaged sensitivity function $\overline{S_c}(f)$ by averaging the sensitivity functions obtained. The uncalibrated acoustic waveforms were pre-amplified at either 30 dB or 60 dB (for detection purposes); therefore, de-amplified waveforms, $I_d(f)$, were first calculated to correct for the appropriate amplification level. Then, calibrated acoustic waveforms $I'_d(f)$, with a unit of velocity (m/s), were obtained in the frequency domain by deconvolution of the waveforms measured by the AE transducer $I_d(f)$ and the sensitivity function, $\overline{S_c}(f)$. These were also normalized using the transducer's sensitivity S_t:

$$I'_d(f) = \frac{I_d(f)}{S_t \overline{S_c}(f)}. \tag{2}$$

In order to estimate seismic parameters such as corner frequency and stress drop, we used S-wave displacement spectra, the transducer used being polarized for transverse motion, that is, for S-wave detection. AE waveforms were analyzed within a 27.5 µs time window beginning 2.5 µs before the S-wave arrival times, which were picked manually. This time window was then rescaled to a 50 µs time window centered on the S-wave arrival time and multiplied by a von Hann window. We obtained S-wave displacement spectra $\Omega_s(f)$ by first deconvolution of the AE waveforms $I'_d(f)$ out of the sensitivity function $\overline{S_c}(f)$. Final displacement spectra were thus obtained by integration in frequency space. This takes the following form:

$$\Omega_s(f) = \frac{I'_d(f)}{\overline{S_c}(f)} \cdot \frac{1}{2\pi f}. \tag{3}$$

S-wave displacement spectra were then fitted with a Brune model corrected for attenuation (Brune, 1970). The S-wave displacement spectra $\Omega_s(f)$ were modeled as:

$$\Omega_s(f) = \Omega_0 \exp(\pi f t / Q) \cdot \frac{1}{1 + (f/f_c)^2}, \tag{4}$$

where Ω_0 is the long-period amplitude, t is the S-wave travel time, Q is the attenuation factor, and f_c is the corner frequency. Ω_0, Q, and f_c were estimated by a grid search over the three parameters. If Q and f_c were simultaneously estimated from the spectrum, a trade-off between Q and f_c could arise. Therefore, we first estimated a unique Q value by a pre-grid search of Ω_0 from 10^{-22} to 10^{-15} over intervals of $10^{0.5}$ ms, Q from 10 to 200 over intervals of 5, and f_c from 0.1 to 10 MHz over intervals of 0.05 MHz. We selected the most frequent Q value in a Q distribution obtained from the S-wave displacement spectra in each sample. The selected Q values are listed in Table S3 in Supporting Information S1. Next, under these Q values, we estimated Ω_0 and f_c by a grid search of Ω_0 from 10^{-21} to 10^{-16} over intervals of $10^{0.01}$ ms and f_c from 0.1 to 10 MHz over intervals of 0.01 MHz. We excluded results for which the estimated Ω_0 or f_c reached the upper or lower limit for the search. The seismic moment (M_0) was calculated from Ω_0:

$$M_0 = \frac{4\pi \rho V_s^3 R \Omega_0}{R_{\theta,\phi}}, \tag{5}$$

where ρ is the density, 3.97×10^6 g/m^3 for germanate olivine (Liebermann, 1975), V_s is the S-wave velocity, 4,220 m/s for germanate olivine (Liebermann, 1975), R is the distance between the source and the transducer, and $R_{\theta,\phi}$ is the averaged radiation pattern coefficient, 0.63 (Aki & Richards, 2002). The moment magnitude (M_w) was calculated from the seismic moment (M_0):

$$M_w = (\log M_0 - 9.1)/1.5. \tag{6}$$

Eventually, b-values of the Gutenberg-Richter law were estimated by the maximum likelihood method (Aki, 1965; Utsu, 1974), the Gutenberg-Richter law being expressed as follows (Utsu, 1974):

$$\log n(M) = a - bM. \tag{7}$$

where $n(M)$ is the number of earthquakes having magnitude over M. a and b are constants.

2.4. Microstructural Observation

All deformed samples and starting materials were cut in half along the direction of compression and impregnated with epoxy to analyze the microstructures. Samples were polished with diamond paste and colloidal silica suspension and observed with field-emission scanning electron microscopes: JEOL 7001F (Tohoku University),
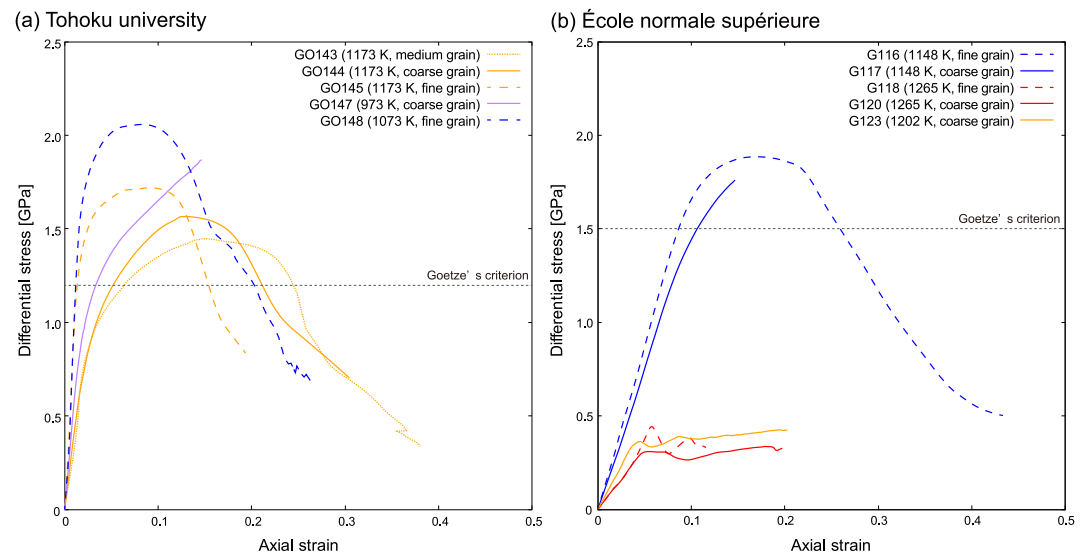
Figure 4. Stress-strain curves of deformation experiments performed at Tohoku University (a) and École Normale Supérieure (b). Dashed, dotted, and solid lines show experiments on fine-, medium- and coarse-grained aggregates, respectively. Black dashed line shows Goetze's criterion. (a) Confining pressure and strain rate are 1.2 GPa and 1.0×10^{-4} s^{-1}, respectively. (b) The confining pressure is 1.5 GPa. Strain rate is $4.2 \times 10^{-5} - 1.6 \times 10^{-4}$ s^{-1}; see Table 1.

electron backscatter diffraction (EBSD, Oxford instruments installed at Tohoku University), ZEISS Zigma (ENS), and Zeiss Gemini 1530 (University of Bayreuth). The step size for EBSD maps varied from 0.5 to 10 μm depending on grain size. EBSD data were analyzed using the MTEX MATLAB toolbox (Bachmann et al., 2010; Hielscher & Schaeben, 2008). Grain boundaries were determined using a threshold misorientation angle of 10°. Grain size distribution and CPO were constructed from one point per data.

Samples GO143, GO144, and GO145 were also observed with a scanning transmission electron microscope (TEM, Philips CM20FEG, and FEI Titan G2 80–200 S/TEM) at University of Bayreuth with an accelerating voltage of 200 kV. TEM analysis was made on a foil from a thin section of GO143, GO144, and GO145 obtained with a dual-beam focused ion beam milling machine (FIB, FEI Scios, University of Bayreuth).

3. Results

3.1. Mechanical Data

Samples deformed at low temperatures (973–1,173 K) had high peak stresses above Goetze's criterion and large subsequent strain weakening, whereas samples deformed at high temperatures and lower strain rates (1,202 and 1,265 K) had lower peak stresses and negligible strain weakening (Figure 4). Sample GO144 was quenched when the thermocouple broke after approximately 30% shortening, while deformation of sample GO147 was stopped because the axial stress reached the failure strength of the tungsten carbide piston (σ_1 piston). During deformation of both samples G117 and G120, the σ_1 piston broke down, the stress at failure during G120 being much smaller than that in G117. In sample GO148 (1,073 K, fine grain), stick-slip behavior was observed at low differential stress after reaching peak stress ($\varepsilon > 0.2$). Small stick-slips were also observed after reaching peak stress in sample G120 (1,265 K, coarse grain).

3.2. AE Event

Strain weakening of sample G116 corresponds to a series of rapid stress drops (Figures 5a and 5c). Before the first stress drop (enlarged view in Figure 5c), only a few small AEs were collected. Then, after the first stress drop at $\varepsilon \sim 0.24$, a large number of AEs was recorded during the entire strain weakening phase (Figure 5c), resulting in the increase in cumulative moment magnitude (orange dashed line in Figure 5a). AEs with large moment magnitudes ($M_w \geq -7.0$) occurred over a wide range of S-P intervals, although most of these events occurred in the lower part of the sample (small S-P intervals, Figure 5c). In experiment G117 (1,148 K, coarse grain), high AE
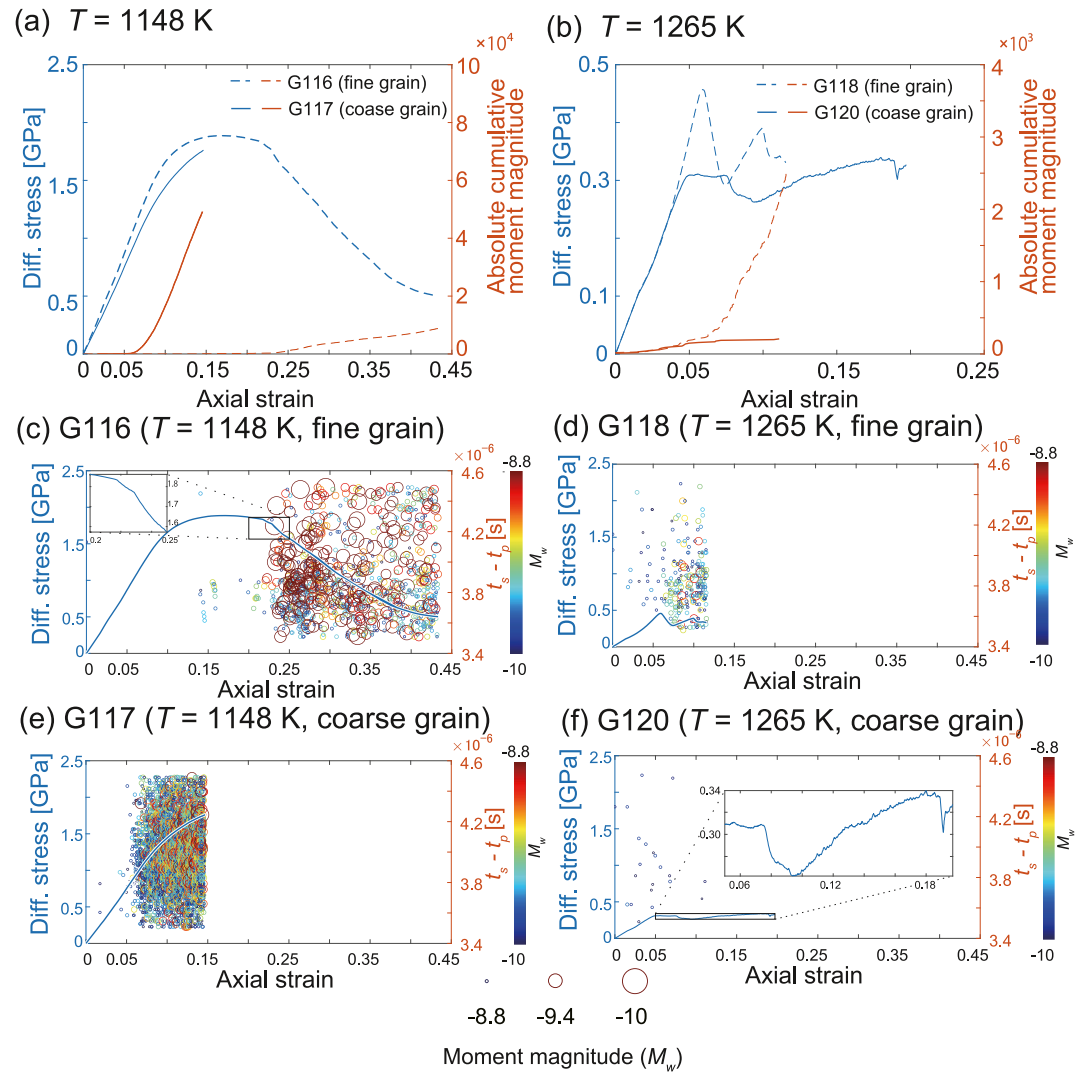
Figure 5. Stress-strain curves (blue lines) and the associated cumulative moment magnitude (orange lines) in the experiments at low (a) and high temperatures (b). Stress-strain curves, S-P intervals ($t_S − t_P$ [s]), and moment magnitudes of deformation experiments (c) G116, (d) G117, (e) G118, and (f) G120. S-P intervals of each acoustic emissions (AE) event are plotted as circles at ranges from 3.5 μs to 4.5 μs. The size and color of the circles show the moment magnitudes of each AE event.

activity started before peak stress (Figures 5a and 5e). The increase rate of moment magnitude was constant and higher than that in experiment G116. In experiment G118 (1,265 K, fine grain), a few AEs occurred before peak stress (orange dashed line in Figure 5b). The AE rate increased after peak stress, and relatively large AEs occurred during strain hardening (approximately $0.07 \leq \varepsilon \leq 0.10$ in Figures 5b and 5d). Small AEs occurred upon the second strain weakening (approximately $\varepsilon = 0.10$ in Figure 5b). In experiment G120 (1,265 K, coarse grain), AEs were far less numerous than in G117. Most AEs occurred before peak stress (orange solid line in Figure 5b). Only a few AEs were detected after peak stress, accompanying the small stress drops that took place (enlarged view in Figure 5f).

The b-values (i.e., the slope of the of the Gutenberg-Richter power law distributions obtained in each experiment) obtained depend both on grain size and temperature (Figure 6). We use $M_w = −10$ as a magnitude of completeness, which corresponds to a kink in the Gutenberg-Richter distribution at smaller magnitude.

For experiments run at 1,148 K (Figures 6a and 6b), larger AEs occurred in the fine-grained aggregate (G116). Conversely, smaller AEs occurred more frequently in the coarse-grained aggregate specimen (G117). Hence, b-values of 0.63 and 1.20 were in G116 and G117, respectively. At 1,265 K (Figures 6c and 6d), the b-values of
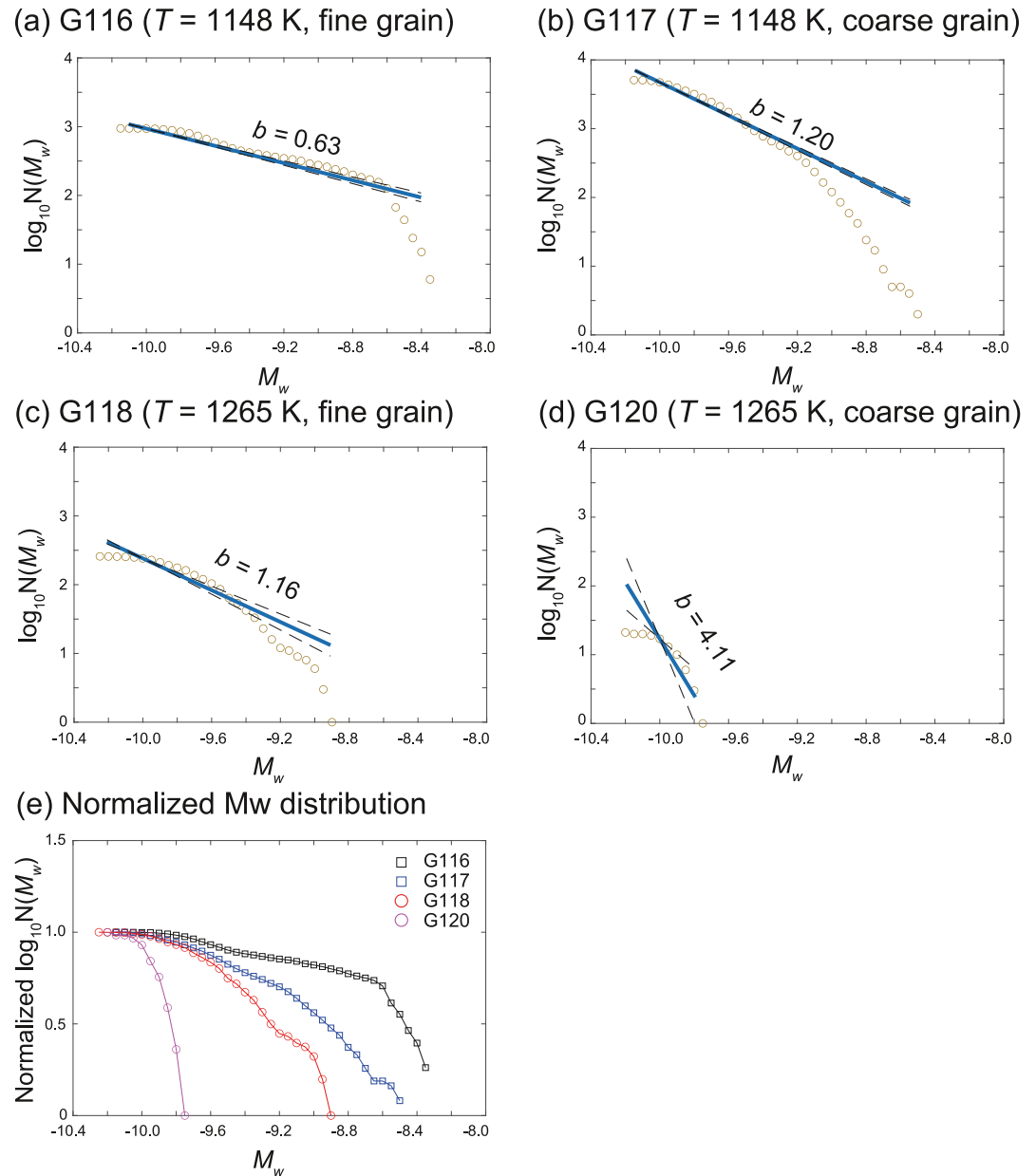
Figure 6. (a–d) Frequency-magnitude distributions (orange circles) for experiments G116, G117, G118, and G120 and b-values (slope of solid blue lines) estimated by maximum likelihood method for $M_w \geq -10$. Dashed lines show the 95% confidence interval of the obtained b-values. (e) Corresponding normalized frequency-magnitude distributions.

1.16 and 4.11 were obtained for the fine- (G118) and coarse-grained aggregates (G120), respectively, that is much larger than the b-values at lower temperatures (1,148 K). Note however that the standard error is large for the b-value of G120 because of the small number of AEs. The nomalized M_w distribution plot (Figure 6e), demonstrates the combined effects of grain coarsening and temperature increase, both of which tending to inhibit the nucleation of larger fractures. b-values are summarized in Table 1.

Stress drops retrieved across all experiments combined (Figure 7) range from 1 kPa to 100 MPa. Stress drops $\Delta\sigma$ can be calculated from M_0 and source radius r as $\Delta\sigma = 7M_0/16r^3$ (Eshelby, 1957), where $r = 0.21V_s/f_c$ (Madariaga, 1976). First, experiments performed at low temperature (G116 and G117) exhibit larger stress drops, which is consistent with the fact that AEs were produced under larger macroscopic stress during these. Conversely, AEs produced at higher temperature (G118 and G120) exhibit lower stress drop in average for a
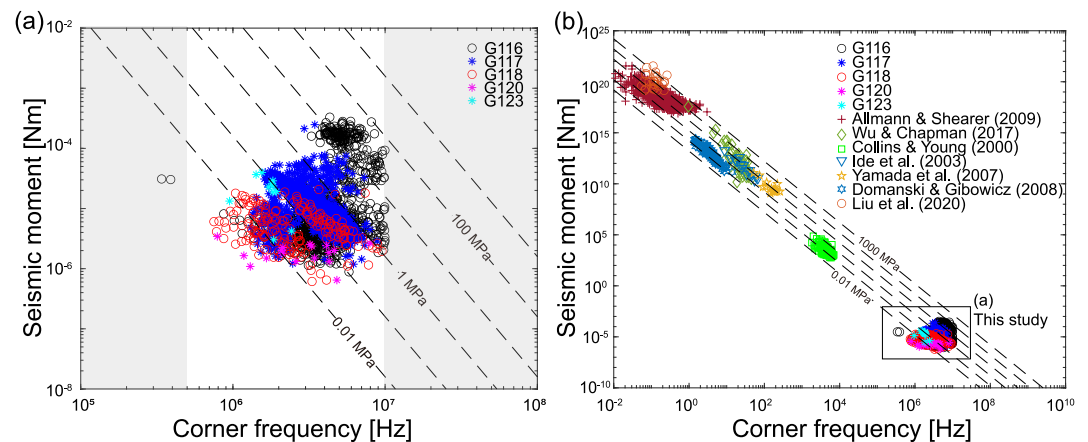
Figure 7. Relationship between seismic moment M_0 and corner frequency f_0. Dashed lines show stress drops of 0.01, 0.1, 1, 10, 100, and 1,000 MPa from Madariaga's source model (Madariaga, 1976). (a) Relationship between M_0 and f_0 estimated from this study. The gray-colored regions show an undetectable frequency range in our acoustic emissions setting (∼500 kHz and ∼10 MHz). The same relationship is presented in greater detail, including error bars, in Figure S4 in Supporting Information S1. (b) Relationship between M_0 and f_0 from this study and previous studies (Allmann & Shearer, 2009; Collins & Paul Young, 2000; Domański & Gibowicz, 2008; Ide et al., 2003; Liu et al., 2020; Wu & Chapman, 2017; Yamada et al., 2007).

similar reason. Second, large AEs (i.e., with large seismic moments) tend to have larger stress drops, which might either be real or an artifact due to a finite size effect of our specimen.

Corner frequencies ranges from 10^6 Hz to 10^7 Hz, corresponding to source sizes ranging between 90 and 900 μm. Experiments at 1,148 K (G116 and G117) exhibit high corner frequencies (around 10^7 Hz, small source sizes) with large stress drops. Meanwhile, the experiments at 1,202 and 1,265 K produced AEs with smaller seismic moments and a wide range of corner frequencies with small stress drops.

3.3. Microstructure of Deformed Samples

3.3.1. SEM Analysis

Many faults containing fine-grained germinate spinel show localized deformation (Figures 8 and 9). In sample GO145 (1,173 K, fine grain), a fault (red arrows) with an offset of 70 μm is observed with spinel aggregates in the lower right part of the sample (Figure 8a; Figure S5a in Supporting Information S1). A small fault sub-parallel to the large fault cut the pyroxene grain sharply (orange arrows in Figure 8a). In sample GO148 (1,073 K, fine grain), bands of spinel near the fault sheared relatively coarse-grained pyroxene (red arrows in Figure 8b, spinel bands, discussion later in Section 3.3.2). These bands were composed of fine-grained germanate spinel recrystallized into small euhedral grains and cut through multiple germanate olivine grains (red arrows in Figure 8c). Many faults with clear offsets composed of fine-grained germanate spinel (orange arrows in Figure S5e in Supporting Information S1 and red arrows in Figure 8d) cut/shear the pyroxene grains in sample G116 (enlarged view in Figure S6 in Supporting Information S1). In sample G118 (1,265 K, fine grain), a fault was observed on the right side of the sample (orange arrow in Figure S5g in Supporting Information S1), although platinum derived from the capsule penetrated the lower part of the sample.

No through-going faults were observed in sample GO143 (1,173 K, medium grain, Figure S5b in Supporting Information S1). However, spinel bands align sub-parallel to each other inside the same grain and cut through pyroxene inclusions (red arrows in Figure 9a). Additionally, spinel lenses perpendicular to the maximum compression direction were observed (red arrows in Figure 9b). These spinel lenses developed inside germanate olivine grains. In sample GO144 (1,173 K, coarse grain), spinel bands were observed near the crack in the center (red arrows in Figure 9c). These spinel bands also developed sub-parallel to each other inside grains. Furthermore, a thin spinel band cut through a pyroxene grain with an offset of 2 μm (orange arrow in Figure 9d). In sample G117 (1,148 K, coarse grain), a large, oblique fault with a clear offset of 100 μm was
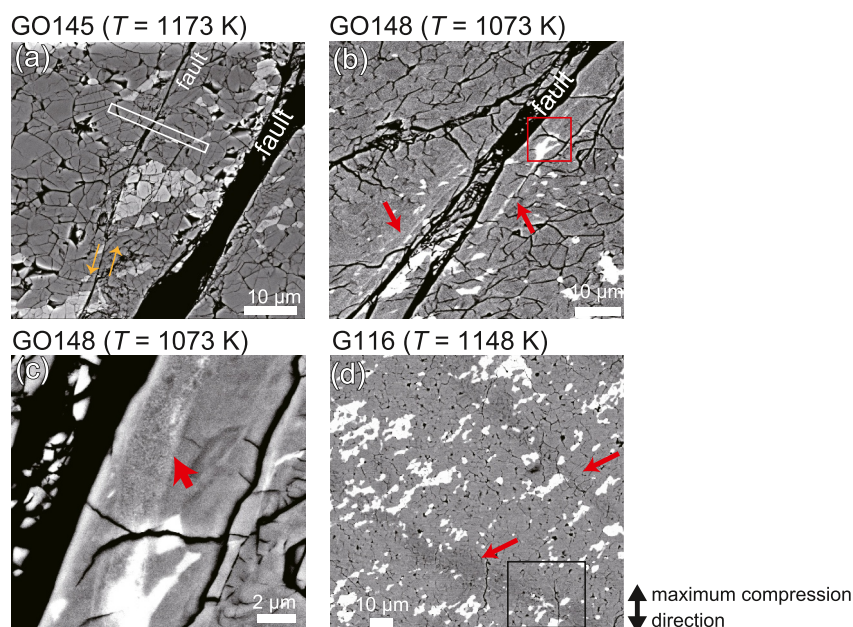
Figure 8. Back-scattered electron images of fine-grained aggregates: GO145 (a), GO148 (b, c), and G116 (d). The maximum compression direction is vertical on all of the images. The dark gray grains are germanate olivine, and the brightest ones are germanate pyroxene. The light gray grains are germanate spinel bands (shown by red arrows). Orange arrows show small faults. White rectangles show where FIB foils were cut. Images a, b, and d correspond to the blue box in Figures S5a, S5d, and S5e in Supporting Information S1, respectively. (c) The image corresponds to the red box in (b). (d) The black box corresponds to Figure S6 in Supporting Information S1.
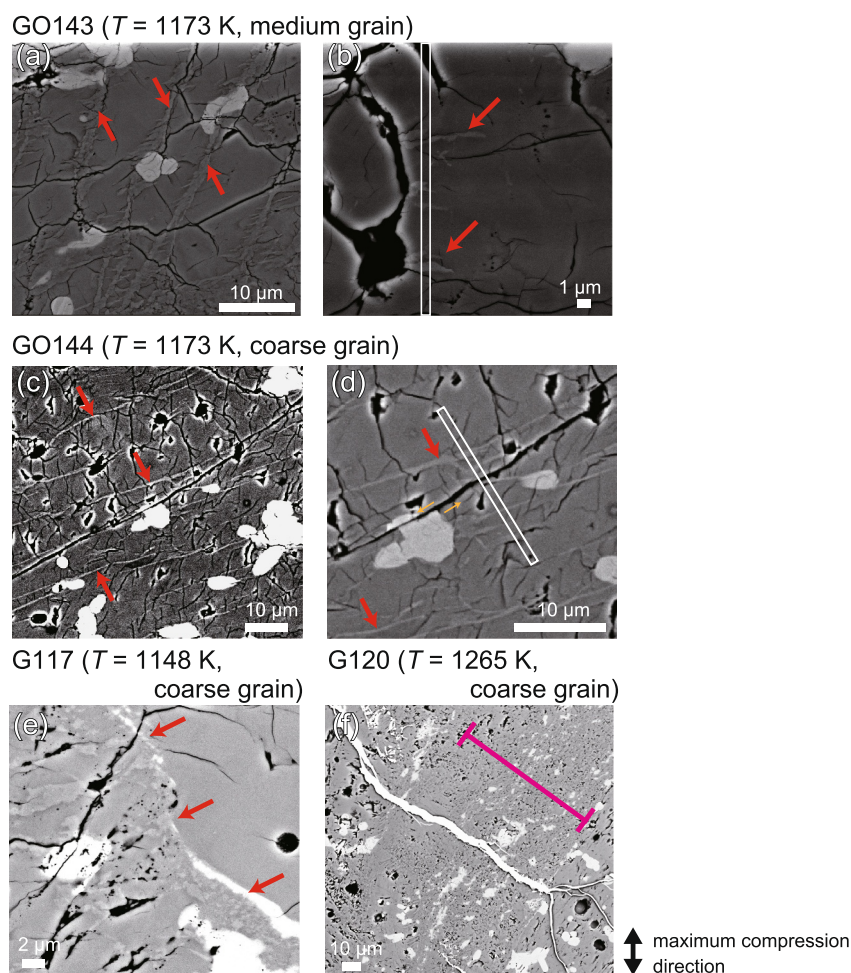
observed (orange arrow in Figure S5f in Supporting Information S1). Spinel is present in shear bands where shear is demonstrated by stretching of pyroxene grains (red arrows in Figure 9e). In sample G120 (1,265 K, coarse grain), a thick oblique shear band with a clear offset of 150 µm can be observed at the upper part of the sample (orange arrow in Figure S5h in Supporting Information S1), although platinum also penetrated the lower part of the sample. The width of the shear band is approximately 60 µm (pink line in Figure 9f). The shear band sharply cut surrounding minerals; it is composed of fine-grained minerals, including many pyroxene grains that were intensely sheared.

Final volume fractions of spinel estimated from SEM analysis are listed in Table 1. The distribution of spinel grains is heterogeneous (e.g., in sample G116, the volume fraction of spinel is larger in the lower part). The volume fraction reported here is calculated from SEM images with the highest fraction of spinel grains. Samples held at a temperature of 1,148–1,173 K for 39–71 min have a volume fraction of almost 10%. Samples that experienced 1,173–1,202 K for 98–168 min have 24%–28% spinel. At 1,265 K, the volume fraction of spinel for 34–42 min reaches 21%–22%.

3.3.2. TEM Analysis

Figure 10 shows scanning TEM images of FIB foils extracted from the locations shown by white rectangles in Figures 8 and 9. In GO145 (1,173 K, fine grain), a fault was observed at the center of the FIB foil (Figures 10a and 10b). The germanate olivine grains across the fault have different crystallographic orientations, as demonstrated when comparing the selected area electron diffraction (SAED) patterns from the two grains (Figure S7 in Supporting Information S1). Fine-grained minerals with a grain size of less than 50 nm were observed along the grain boundary of germanate olivine (blue box in Figure 10a). SAED pattern taken from the fine-grained core of the fault shows that it is made of germanate spinel, as shown by the Debye rings of germanate spinel (red and green arrows in Figure 10) corresponding to the {220} and {311} reflection with d-spacings of 0.292 and 0.249 nm, respectively (Dachille & Roy, 1960). In sample GO143 (1,173 K, medium grain), the high-angle annular dark-

GO143 (*T* = 1173 K, medium grain)

GO144 (*T* = 1173 K, coarse grain)

G117 (*T* = 1148 K, coarse grain) G120 (*T* = 1265 K, coarse grain)


Figure 9. Back-scattered electron (BSE) images of medium- and coarse-grained aggregates: GO143 (a, b), GO144 (c, d), G117 (e), and G120 (d). The maximum compression direction is vertical on all of the images. In BSE images, contrast was enhanced so that germanate pyroxene grains (as well as the platinum capsule) appear white. The gray regions are mostly germanate olivine, with some spinel that appears in a slightly brighter shade of gray. Red arrows point toward strain localization regions that contain spinel bands. Images a, c, e, and f correspond to the blue boxes in Figures S5b, S5c, S5f, and S5h in Supporting Information S1, respectively. Image b corresponds to the red box in Figure S5b in Supporting Information S1. (d) An enlarged view of (c). (f) Pink lines show the thickness of the shear band.

field image shows spinel lenses observed in Figure 9b (red arrows) and diagonally developed bands composed of fine-grained spinel (white arrows in Figure 10d). A close-up view of these latter spinel bands is shown in Figure 10e and reveals their extremely thin nature (orange arrows in Figure 10e). The SAED pattern reveals their topotactic relationship to the host grain (Figure 10f): the weak diffraction spot with a d-spacing of 0.462 nm (white arrow in Figure 10f) can be indexed by $11\bar{1}$ of germanate spinel (Dachille & Roy, 1960). The strong diffraction spots from the host grains with d-spacings of 1.02 and 0.480 nm (yellow arrows in Figure 10f) can be indexed by the 010 and 100 of germanate olivine, respectively (Dachille & Roy, 1960). The strong diffraction spots with d-spacing 0.480 nm can also be indexed by 111 of germanate spinel (Dachille & Roy, 1960). It is parallel to that of the (100) plane of germanate olivine. In sample GO144 (1,173 K, coarse grain), the dark-field (DF) image shows many spinel bands aligned parallel to each other (red arrows in Figure 10g). These fine-grained bands can be as thick as approximately 1 µm. The enlarged view of these spinel aggregates reveals their extremely fine-grained nature (approximately 100 nm, Figure 10h). Furthermore, the angle between the two sets of spinel bands observed is ~72° (Figure 10h). Figure 10i shows the SAED pattern of the host mineral (Figure 10g). The
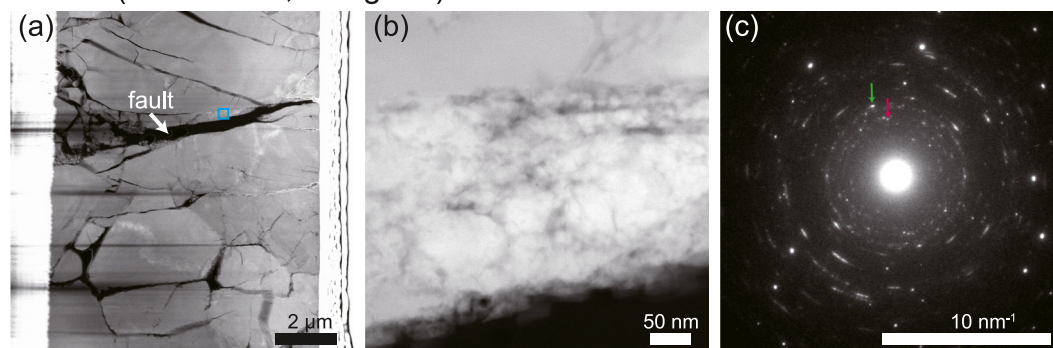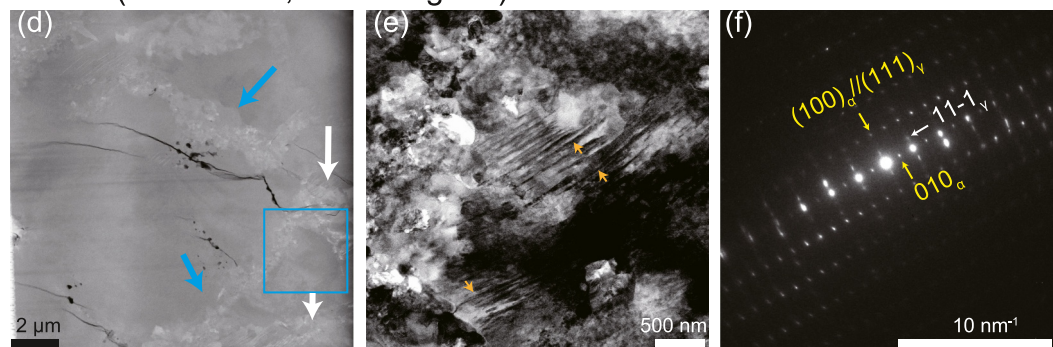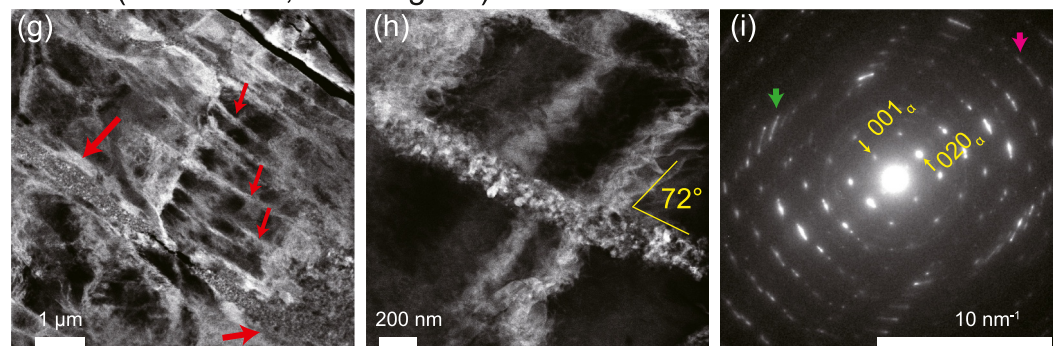
Figure 10. Scanning transmission electron microscope images and electron diffraction patterns: (a) high-angle annular dark-field (HAADF) image of GO145 in a FIB foil located by the white rectangle in Figure 8a. The right side of the foil corresponds to the polished surface in Figure 8a. Gray and light gray minerals are germanate olivine and germanate pyroxene, respectively. (b) HAADF image corresponding to the blue box in (a). The core of the fault, at the bottom of the image, consists of extremely fine-grained gouge made of brighter grains (c) Selected area electron diffraction (SAED) pattern of the fault core in (b), which shows mostly germanate spinel. The rings shown by red and green arrows correspond to the {220} and {311} reflections of germanate spinel, respectively. (d) HAADF image of GO143 in a FIB foil (white rectangle in Figure 9b). Gray and light gray minerals are germanate olivine and germanate spinel (blue arrows), respectively. White arrows point to the spinel lenses visible in Figure 9b. (e) Bright-field (BF) image corresponding to the blue box in (d). Orange arrows show stacking faults in an olivine grain. (f) SAED pattern corresponding to lamellae in (e), evidencing topotactic coexistence of olivine (α, by greek symbol) and spinel (γ, by greek symbol). (g) Dark-field (DF) image in a FIB foil extracted from sample GO144 (white rectangle in Figure 9d). Red arrows show spinel bands in an olivine grain. (h) DF image corresponding to spinel bands in (g). (i) SAED pattern corresponding to a host olivine grain in (g) and taken along the [100] zone axis. Green and pink arrows show the split set of spots from olivine.

spots with d-spacings of 0.51 and 0.59 nm can be indexed by the 020 and 001 of germanate olivine, respectively (Dachille & Roy, 1960). The split set of spots shown by a green arrow shows approximately 10° of angular misorientation, while that shown by a pink arrow shows approximately 3° of angular misorientation.

4. Discussion

4.1. Mechanism of the Olivine-Spinel Phase Transformational Faulting

During deformation experiments, phase transformation from germanate olivine to spinel occurred either at the grain boundaries and within grains. At the scale of the sample, transformation is usually more advanced near the top alumina piston, due to the stress concentration it creates in the sample (Cionoiu et al., 2019, 2022; Gasc, Gardonio, et al., 2022). These large spinel-rich regions largely contributed to the deformation of the entire sample (e.g., Figures S5b and S5c in Supporting Information S1) and may have contributed to the eventual faulting of some samples. Both volume reduction (8.1%) due to the phase transformation and a lower flow strength of the newly created spinel compared to that of olivine may have enhanced the deformation of the samples observed in the transformed regions. The microstructures observed therefore show a tendency for strain and transformation to localize together, as previously reported in other experimental studies (Holyoke & Tullis, 2006) and numerical simulations (Baïsset, Yamato, & Duretz, 2024). As a result of the stress relaxation experiment on sample G123 (Text S2 in Supporting Information S1), the stress exponent is 4.14, indicating that the deformation mechanism is dislocation creep at high temperature. We hypothesized that the deformation mechanism was dislocation creep in all samples and calculated the strength of germanate olivine and spinel based on the following flow laws for dislocation creep (Shi et al., 2015):

$$\dot{\varepsilon} = A\sigma^n \exp\left(-\frac{Q}{RT}\right), \tag{8}$$

where A is a constant, σ is the flow stress, n is the stress exponent, and Q is the activation energy. According to Shi et al. (2015), $A = 10^{5.01}$ MPa^{n}s^{-1}, $n = 3.1$, $Q = 441$ kJ/mol for germanate olivine, and $A = 10^{-3.4}$ MPa^{n}s^{-1}, $n = 2.9$, $Q = 228$ kJ/mol for germanate spinel. For example, in GO143, strain rate and temperature were 10^{-4} s^{-1} and 1,173 K, respectively, and the corresponding strengths of olivine and spinel were estimated to be 3,380 and 2,510 MPa, respectively. This indicates that spinel is weaker than olivine under these conditions, in agreement with the observed strain localization on large spinel-rich regions. Therefore, the buckling observed in some samples is likely the result of this local weakening as well as from the volume reduction associated with the transformation. For instance, in sample GO143, shortening was the largest on the left side of the sample, where the fraction of spinel grains is the largest. Spinel nucleation along the left side of the platinum capsule may have started earlier than along the other side due to a slight temperature difference. Further development of spinel aggregates was then promoted thanks to the latent heat release of the phase transformation itself, which tends to initiate a positive feedback loop when far from equilibrium (Kirby, 1995). In sample G116, we observed rigid body rotation caused by faulting that occurred at approximately 45° to the sample's long axis. After the initial faulting, the stress was predominantly supported by one side of the sample, leading to subsequent rotation of the faults. This rigid body rotation altered the contact area between the sample and the deformation piston, which affects the axial stress measurements. Our AE data, demonstrate that faulting, and therefore sample rotation occurred during the final stages of deformation. Therefore, although this does not impact our primary findings, the mechanical part of the curve beyond the peak stress does not reflect the strength of the fault or of the bulk of the sample.

In fine-grained samples, phase transformation was observed in fault planes, where spinel did not have a specific orientation to the maximum compression direction (Figure 10b). Meanwhile, two types of intracrystalline spinel grains were observed, both preferentially elongated normal to the principal stress inside medium and coarse olivine grains: lenses with lengths of a few microns (Figures 9a and 9b) and thin lamellae that cross entire grain widths ($l > 100$ μm, Figures 9c and 9d). The first type is characterized by the incoherent growth already reported by Burnley et al. (1991). We also noted the presence in the vicinity of the lenses of intracrystalline spinel lamellae within the olivine grains, characterized by an alignment of the (111) plane of spinel parallel to the (100) plane of the host olivine (Figures 10e and 10f). These features have been reported in silicate olivine by Kerschhofer et al. (1996) who proposed that spinel (ringwoodite) lamellae coherently nucleated on stacking faults in olivine; they were shown to be a martensitic transformation mechanism by Burnley (2005) in the germanate olivine-spinel transformation. The second type of transformation is characterized by fine-grained spinel nucleation along (010) and (011) of olivine (Figures 10g and 10h). Most of these fine-grained spinel aggregates are sub-parallel to the (010) plane of the olivine host. Spinel grains were also formed along the (011) plane of olivine and show an

apparent tilt angle of 72° relative to the (010) plane. This observed angle deviates from the theoretical crystallographic angle of 59.7° between these planes in perfect olivine crystals. The discrepancy between 59.7° and 72° may simply reflect the angular misorientation within olivine grains, which can reach approximately 10° (Figure 10i). This mechanism of phase transformation is consistent with preferred spinel nucleation on the kink bands described by Burnley et al. (2013) as well as with the one proposed by Riggs (2005). In the microstructures taken along the [100] zone axis (Figure 10g), the crystal was slightly rotated around the [100] direction (Figure 10i). This microstructure is similar to the kinked ones already shown by Burnley et al. (2013) in germanate olivine. Burnley et al. (2013) reported that the kinks were formed by rotation about the [010] direction in germanate olivine grains deformed at 1,000–1,473 K and 0.6–1.3 GPa. It is possible that olivine grains observed in this study also deformed by kinking around the [010] direction and that spinel aggregates formed as a result of dislocation pileups and kinks in these grains.

These fine-grained spinel bands were observed in all coarse-grained samples. Riggs (2005) and Wang et al. (2017) reported these spinel bands as nano shear bands, and likely the growth products of slip bands in (010) and (011) planes of olivine. Furthermore, they pointed out that nano shear bands also develop from the tips of regions where localized volume reduction occurred, such as anticracks and spinel nucleation at the grain boundaries. Meanwhile, Gasc, Daigre, et al. (2022) showed that these spinel bands can be the result of dynamic fault propagation (rather than their cause), as suggested by the presence of frictional melt products. Their microstructural observations showed submicronic euhedral spinel grains. Faulting generates additional heat that can produce frictional melt. Pressure and temperature conditions were those of the spinel field. Consequently, since high temperature conditions preclude quenching a glassy (i.e., amorphous) melt product, frictional melt recrystallized as fine-grained spinel. Ohuchi et al. (2022) performed deformation experiments on silicate olivine at 11–17 GPa and 860–1,350 K and also reported melt microstructures in the fault gouge consisting of olivine and wadsleyite. In the fine-grained olivine of this study, fine-grained spinel aggregates were observed at the grain boundaries, whereas spinel was not observed inside olivine grains (Figure 10b). Therefore, fine-grained spinel aggregates at the grain boundaries act as localized volume reduction, conducive to faulting, which, in turn, produces a local heat rise and in some cases frictional melting, responsible for the observed spinel bands (Figures 8c and 8d). Sample G118 displays two distinct mechanical weakening events (Figure 5d). These events appear to correlate with the development of a primary macroscopic fault (orange arrow in Figure S5g in Supporting Information S1) and a secondary fracture zone. Although platinum intrusion partially obscured microstructural evidence, mechanical data and preserved structures suggest the sequential development of conjugate faulting features. In the coarse-grained samples, spinel aggregates were observed along (100), (010), and (011) planes of olivine grains (Figure 10c). These spinel aggregates behave as localized volume reduction and result in faulting. As a result, the spinel bands observed can be formed due to frictional heat.

Faulting occurs in germanate olivine aggregates at moderate temperatures ($1,100 \text{ K} < T < 1,200 \text{ K}$), while deforming by semi-brittle mechanisms (dislocation glide + cracking; Figure 11). This unusual behavior indicates that strain localization, and eventual faulting, requires the olivine-spinel phase transformation as proposed by previous studies (Burnley et al., 1991; Gasc, Daigre, et al., 2022, Gasc, Gardonio, et al., 2022; Green & Burnley, 1989; Green et al., 1992; Riggs, 2005; Schubnel et al., 2013; Tingle et al., 1993; Wang et al., 2017). Phase transformation is a thermally activated process that promotes strain localization at high temperatures. At >1,200 K faulting occurred despite low sample strength, although AE counts were far lower than at moderate temperatures. At temperatures <1,200 K, brittle fracture is the dominant microscopic mechanism leading to strain localization. These brittle fractures were observed as numerous AEs. The occurrence of phase transformation in conjunction with brittle fractures generates a lot of latent and frictional heat, and strain (elastic strain energy) around the localized region, which promotes further phase transformation and subsequent localization. Elastic strain hinders phase transformations, but the plastic strain caused by the phase transformation itself releases the elastic strain energy, keeping the progress of the phase transformation (Liu et al., 1998; Sawa et al., 2023). Finally, this positive feedback results in macroscopic brittle faulting that produces frictional melting. Fine-grained spinel nucleates during the cooling of the frictional melt products, thus forming the long and thin spinel bands observed (Figure 8c). At high temperatures, plastic flow is enabled and brittle fractures are inhibited (Figure 11). Therefore, at >1,200 K, mylonites were observed instead of large faults with frictional melt (Figure 8d, resulting in a small number of AEs.
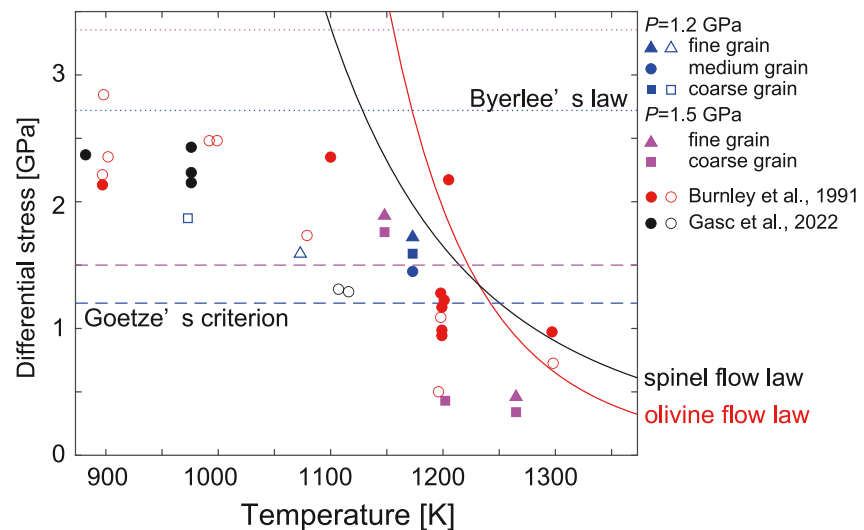
Figure 11. Plots of sample strength versus temperature in this study and previous ones (Burnley et al., 1991; Gasc, Gardonio, et al., 2022). Open symbols show ductile behavior; Filled symbols show faulting. Blue and purple dashed lines show Goetze's criterion at confining pressures of 1.2 and 1.5 GPa, respectively (Kohlstedt et al., 1995). Blue and purple dotted lines show Byerlee's law at confining pressures of 1.2 and 1.5 GPa, respectively (Byerlee, 1978). The red and black solid lines show flow laws for dislocation creep of germanate olivine and spinel (Equation 8) at a strain rate of 1.0×10^{-4} s^{-1} (Shi et al., 2015).

4.2. AE Activity and *b*-Value Dependence on Olivine Grain Size

Absolute cumulative moment magnitude provides a more direct measure of the total energy released during deformation. While AE counts give insight into the frequency of microcracking events, the moment magnitude better reflects the mechanical significance of these events. A few high-magnitude AEs can release equivalent or greater energy than numerous small-magnitude events, and this energy release directly correlates with observed stress drops in our mechanical data. Some AEs may originate from cell parts such as fired pyrophyllite and graphite. However, Baïsset, Labrousse, et al. (2024), using identical cell assemblies and AE settings, reported minimal AE activity at high temperatures when their samples deformed in a ductile manner (e.g., <23 events at 1,073 K). Given that our experiments were conducted at even higher temperatures (≥1,148 K), we expect the contribution from cell parts to be negligible. Therefore, we conclude that the vast majority of detected AEs in this study originate from the olivine sample. The observed AEs likely originated from both phase transformation-induced faulting and cracking processes that occurred at peak stresses above the Goetze criterion. In experiment G116, some AEs were generated immediately after reaching the Goetze criterion, suggesting a crack-related origin. However, AE activity continued even after the stress dropped below the Goetze criterion. This sustained AE generation suggests that the majority of AEs originated from phase transformation-induced faulting. Also, the effect of Pt intrusion into the samples on the AE measurements can be considered negligible. Pt intrusion was observed only in samples where the deformation pistons were broken. AE measurements were immediately arrested after piston failure. We can detect AEs with seismic moment >10^{-6} Nm. Using stress drop relation above, we can detect the crack with $r \simeq 35$ μm for 10 MPa stress drop and $M_0 = 10^{-6}$ Nm.

The *b*-values in the coarse-grained aggregates are larger than those in the fine-grained ones at the same pressure, temperature, and strain rate conditions (Figure 6). This indicates that *b*-values depend on the grain size of germanate olivine. According to Mogi (1962), in a heterogeneous medium, fault propagation is readily arrested, resulting in a relatively large number of earthquakes with small M_w. Consequently, the *b*-value tends to be high in a heterogeneous medium. Therefore, the span in *b*-values obtained in this study likely reflects variations in heterogeneity of the stress field due to grain size, which also causes differences in phase transformation mechanisms. Spinel grains in the fine-grained samples grow at olivine grain boundaries and develop homogeneously throughout the aggregate. On the other hand, spinel grains in the coarse-grained olivine aggregates do not develop at olivine grain boundaries but appear heterogeneously inside olivine grains at dislocation pileups along (100), (010), and (011) planes or kinking. These observations suggest that spinel bands were formed heterogeneously throughout the sample, reflecting the Schmid factor distribution. The spatial distribution of these spinel grains

determines the distribution of subsequent brittle fracture that accompanies the phase transformation. Therefore, the heterogeneous growth of spinel bands in coarse-grained olivine aggregates produces *b*-values approximately 2 times higher than those from homogeneous spinel distribution in fine-grained aggregates (in the case of low *T*, 0.63 and 1.20, respectively).

At higher temperature, *b*-values are higher in both fine- and coarse-grained aggregates in this study, consistently with previous results (Gasc, Daigre, et al., 2022, Gasc, Gardonio, et al., 2022). The rate of phase transformations increases dramatically with temperature (Cahn, 1956; Kubo et al., 2004). As a result, in the high-temperature experiments, phase transformation was likely completed before strain localization took place, resulting in the lack of large faulting events (small number of AEs with large M_w) and, increasingly larger *b*-values with increasing temperature.

The differences in phase transformation mechanisms, which depend on grain size, control the transformation kinetics, and therefore, the timing of AE activities. In the fine-grained aggregates, AE activities began before peak stress at high temperature, and continued as the deformation progressed (G118, Figure 5b), whereas, at low temperature, AE activities did not start until after peak stress (G116, Figure 5a) despite much higher stress levels. The temperature-dependent timing of AE activities is a direct consequence of AEs being related to strain localization, which is enabled by the phase transformation. Because the transformation progresses more rapidly at high temperature, strain localization occurs at lower strains and stresses, resulting in a myriad of early small AEs (Figures 5b, 5d and 5f). However, in the coarse-grained aggregate and at low temperature, AE activities did start before peak stress (G117, Figures 5a and 5e), that is, sooner than they did in the fine-grained counterpart (G116, Figures 5a and 5c). According to Riggs (2005) and Wang et al. (2017), spinel lenses (localized volume reduction) preferentially develop in large olivine grains. It is therefore likely that in the fine-grained aggregates, localized volume reduction did not occur until the deformation had progressed to a greater amount of strain. AE activities, which are derived from the appearance of these localized volume reduction patches due the local mechanical instability they cause, were consequently delayed until after the peak stress. In coarse-grained olivine aggregates, spinel bands (associated with faulting) were formed as a result of dislocation pileups and kinks along the (010) and (011) planes of olivine grains. These features developed immediately after deformation progressed into the plastic domain, generating AEs during the early stages of deformation.

Differences in P- and S-wave arrival times demonstrate that AE activities concentrated in the center and lower parts of the samples (Figures 5b–5d). This is a consequence of the vertical temperature gradient in the assembly causing the center and lower end of the sample to sit at slightly higher temperatures than the top (Figure S2 in Supporting Information S1). Transformation rates are therefore higher in the center and lower parts of the sample (in sample G116, the volume fraction of spinel is the largest in the lower part of the sample). The highest AE rate was observed slightly below the central portion of the sample, indicating that the temperature at which deformation preferentially localizes could be lower than the calculated peak temperature at the sample center (Table 1).

The relationship between seismic moment and corner frequency obtained from Equations 4 and 5 is reported in Figure 7 along with those of natural earthquakes and previous experimental studies. Stress drops (equivalent to seismic moments under a given corner frequency) at low temperatures tend to be larger than those at high temperatures (Figure 7). The wide range of stress drops calculated does not result from a change in the phase transformation mechanism, which did not change upon temperature. However, the difference in sample strength due to temperature probably caused the observed range of seismic moment and stress drop. We presume that high temperatures decrease the magnitude of stress drops through stress relaxation mechanisms.

Stress drops of deep-focus earthquakes (Liu et al., 2020) are larger than those of shallow ones (Allmann & Shearer, 2009; Collins & Paul Young, 2000; Domański & Gibowicz, 2008; Ide et al., 2003; Wu & Chapman, 2017; Yamada et al., 2007). Some shallow earthquakes reported in Allmann and Shearer (2009) have large stress drops, but they occur in an intraplate context. Unlike large shallow earthquakes, which occur at the decoupled plate interface, deep-focus earthquakes occur in a context where the subducted plate and the overriding mantle are fully re-coupled, which may be one of the reasons why they also display particularly large stress drops (e.g., Frohlich, 1989; Fukao & Kikuchi, 1987; Wyss & Molnar, 1972).
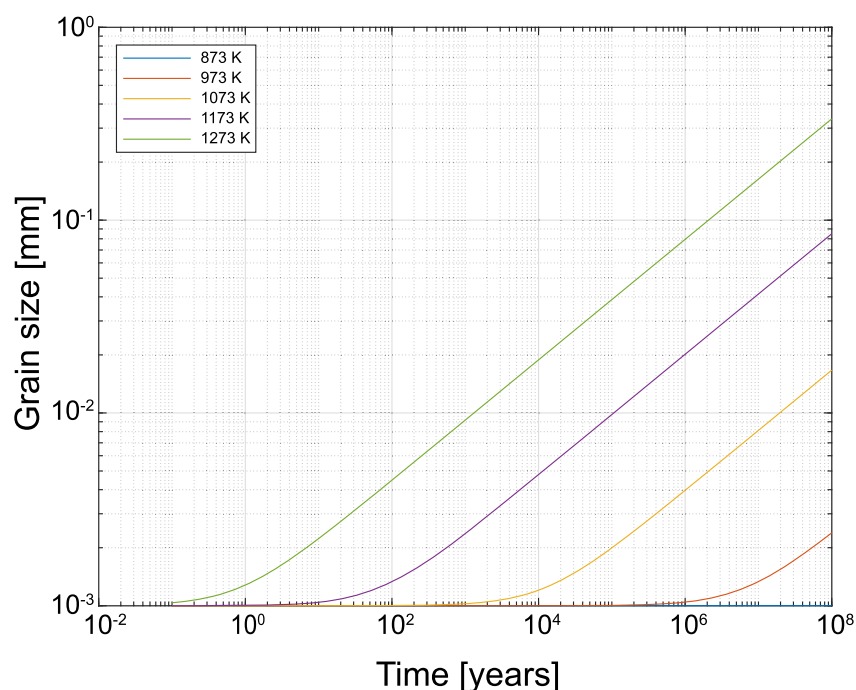
Figure 12. Predicted grain growth curves in fine-grained olivine aggregates using the grain-growth parameter calculated by Speciale et al. (2020). The initial grain size is set to be 1 μm at a pressure of 15 GPa.

4.3. Implication for the Deep-Focus Earthquakes in the Subducted Slab

According to Zhan (2017), in warm slabs with thermal parameters lower than 8,000 km, b-values are 0.49 in the range $5.3 \leq M_w \leq 6.5$, and 0.95 for $6.6 \leq M_w \leq 7.3$. In cold slabs with thermal parameters larger than 8,000 km, b-values are 1.21 for $5.3 \leq M_w \leq 6.5$, and 1.04 for $5.3 \leq M_w \leq 6.5$. To explain the difference in b-values between warm and cold slabs, the author proposed a dual-mechanism hypothesis. In this hypothesis, transformational faulting causes most deep-focus earthquakes in cold slabs, because they contain a thick metastable olivine wedge where rupture by transformational faulting can propagate across large distances two-dimensionally. Consequently, deep-focus earthquakes resulting from transformational faulting alone may explain even the large earthquakes observed in the coldest slabs (e.g., Tonga). The scenario is different in warm slabs, which contain a thin metastable olivine wedge in which deep-focus earthquakes can only propagate by transformational faulting along-strike (1-D rupture geometry). The rupture may continue to grow outside the metastable olivine wedge if the energy released by the rupture is enough to initiate a thermal instability mechanism. The geometry of this thermal-instability rupture would no longer be controlled by the 1-D rupture along-strike the metastable olivine wedge and would thus propagate two-dimensionally. This difference in the rupture geometry affects b-values (Aki, 1981; Hanks & Kanamori, 1979; Kanamori & Anderson, 1975; Wang et al., 2017). However, as Gasc, Daigre, et al. (2022) pointed out, the core of metastable olivine wedge in cold slabs may be too cold to produce transformational faulting deep-focus earthquakes. This is consistent with the observation of a double seismic zone in cold slabs, where ruptures may also be confined to 1-D propagation in thin olivine-ringwoodite transformation fronts surrounding the metastable olivine wedge (Gasc, Daigre, et al., 2022; Wiens et al., 1993). As discussed above, b-values are impacted by grain size (homogeneity) and temperature. In addition to the geometrical constraints on deep-focus earthquake rupture processes proposed by Zhan (2017), we suggest that the homogeneity of the stress field, which tends to increase with temperature, can also control b-values in deep-focus earthquakes. Gasc, Daigre, et al. (2022) indicated that temperature controlled b-values in deep-focus earthquakes. They showed that transformational faulting is controlled by the ratio between strain rates and the transformation rates. As a result of the extrapolation of this relationship to the natural slab conditions, cold slabs with fast subduction rates produced transformational faulting at higher temperatures.

Here, we hypothesize that the metastable olivine wedge of subducted slabs, when present, has intrinsically large stress heterogeneities due to the cold nature of this region, and that the magnitude of these heterogeneities control

b-values. In warm and cold slabs alike, the metastable olivine wedge is possibly made of both fine- and coarse-grained olivine, with grain sizes ranging from a few μm to a few mm derived from outer-rise faults (e.g., Jiao et al., 2000; Silver et al., 1995) and thermal cracks (e.g., Korenaga, 2007). To confirm whether fine-grained olivine derived from outer-rise faults and thermal cracks can be preserved in a metastable olivine wedge, we calculated the grain size evolution of fine-grained olivine based on Speciale et al. (2020) (Figure 12). In grain growth experiments on natural olivine aggregates, Speciale et al. (2020) made the aggregates undergo dynamic recrystallization prior to grain growth. As a result, they revealed that grain boundary migration driven by strain energy due to the deformation delayed the onset of grain growth driven by interfacial energy. In the following, parameters used in the grain growth equation for olivine are a grain growth exponent (*p*) of 3.2, an activation energy (*E_G*) of 620 ± 145 kJmol^{-1}, an activation volume (*V_G*) of 5×10^{-6} m^{3}mol^{-1}, and a rate constant (*k_0*) of 1.8×10^3 m^{p}s^{-1}, respectively. The grain growth equation is the following (e.g., Atkinson, 1988):

$$d_f^p - d_0^p = kt, \tag{9}$$

where *d_f* is the mean grain size at time *t*, *d_0* is the initial mean grain size, and the growth rate *k* follows the relationship:

$$k = k_0 \exp\left(-\frac{E_G + PV_G}{RT}\right), \tag{10}$$

where *P* is the pressure (Pa), *R* is the gas constant $\left(\text{JK}^{-1}\text{mol}^{-1}\right)$, and *T* is the absolute temperature (K). Considering that the highest estimate of temperature inside the metastable olivine wedge of a warm slab to be approximately 1,073 K (e.g., Negredo et al., 2004; Schmeling et al., 1999), 1 μm initial grains of olivine will only reach a radius of approximately 10 μm after 10 Ma (yellow curve in Figure 12), that is, the time required for a warm slab to subduct from the surface to 600 km depth under reasonable subduction rates (∼6 cm/year). In addition, fine-grained olivine derived from outer-rise faulting and thermal cracking will likely have high dislocation density due to the high stress levels and brittle history they were subjected to. Therefore, fine-grained olivine will not only be preserved within metastable olivine wedges in former outer-rise faults for example, but they will also remain weaker regions. Meanwhile, the grain size outside the faults and cracks will become large following the normal grain growth law. Consequently, metastable olivine wedges likely present large strength –and stress– contrasts, resulting from the coexistence of fine- and coarse-grained regions. Gerya et al. (2021) also mentioned that fine-grained regions derived from outer-rise faults can be preserved in the mantle transition zone. Guest et al. (2003, 2004) also evidenced a highly heterogeneous stress field inside the metastable olivine wedge caused by the phase transformation of olivine. Therefore, stress heterogeneities are more than likely generated in all MOW as a result of grain size heterogeneities. This study reveals that transformational faulting occurs independently of grain size, but that the heterogeneity due to the spatial distribution of spinel grains affects *b*-values. In the subducted slab, *b*-values would be controlled not only by temperature (Gasc, Daigre, et al., 2022) but also by how heterogeneous the stress field is. In particular, stress heterogeneity in the metastable olivine wedge is expected to be smaller in warm subducted slab; thus yielding low *b*-values. Meanwhile, cold subducted slabs likely contain more weak damaged regions. This yields both higher stresses and stress heterogeneities in the metastable olivine wedge and results in high *b*-values.

5. Conclusions

We conducted deformation experiments on germanate olivine aggregates containing a small amount of germanate pyroxene with various grain sizes, ranging from a few micrometers to a few hundreds of micrometers. In the fine-grained aggregates, spinel grains at olivine grain boundaries resulted in faulting, forming homogeneous recrystallized spinel bands. In the coarse-grained aggregates, spinel aggregates along (100), (011), and (010) planes of olivine resulted in faulting, forming heterogeneous spinel bands. Thanks to calibrated AE measurements, the scaling law of the phase-transformational faulting observed could be assessed and was shown to follow that of large natural earthquakes. The *b*-values obtained depend on the grain size of olivine; *b*-values in the fine-grained aggregates are smaller than those in the coarse-grained ones at the same deformation conditions. In the coarse-grained aggregates, heterogeneous intracrystalline growth of spinel aggregates leads to high *b*-values. Meanwhile, in the fine-grained aggregates, homogeneous, that is, distributed, growth of spinel

grains at the grain boundaries leads to lower *b*-values. We infer from these observations that the homogeneity (or heterogeneity) of the stress field in which transformational faulting occurs impacts the resulting *b*-values. At the scale of subducted slabs, this is consistent with the range of *b*-values observed, which are correlated to the thermal parameter of the slab (*b*-values being higher for high thermal-parameter slabs). In cold slabs, that is, with high thermal parameter, stresses and therefore stress heterogeneities, are expected to be higher, thus probably contributing to higher-*b*-values. Furthermore, we showed that the preservation of outer-rise faults and thermal cracks as fine-grained regions in the metastable olivine wedge of cold slabs would tend to favor large-scale stress heterogeneities, thus, leading to high *b*-values. In contrast, in warm subducted slabs, faults and cracks from the early stages of subduction are easily healed through recrystallization. The metastable olivine wedge is therefore likely more homogeneous in terms of strength and stress, which, according to our results would promote lower *b*-values.

Data Availability Statement

The data on which this article is based are available in Sawa et al. (2025).

References

Aki, K. (1965). Maximum likelihood estimated of b in the formula log N = a – b*m and its confidence limits (No. 43). https://doi.org/10.15083/0000033631

Aki, K. (1981). A probabilistic synthesis of precursory phenomena. In D. W. Simpson & P. G. Richards (Eds.), *Earthquake prediction: An international review* (Vol. 4, pp. 566–574). American Geophysical Union. https://doi.org/10.1029/ME004p0566

Aki, K., & Richards, P. G. (2002). Quantitative seismology. ui.adsabs.harvard.edu.

Allmann, B. P., & Shearer, P. M. (2009). Global variations of stress drop for moderate to large earthquakes. *Journal of Geophysical Research*, *114*(B1), B01310. https://doi.org/10.1029/2008jb005821

Atkinson, H. V. (1988). Overview no. 65: Theories of normal grain growth in pure single phase systems. *Acta Metallurgica*, *36*(3), 469–491. https://doi.org/10.1016/0001-6160(88)90079-X

Bachmann, F., Hielscher, R., & Schaeben, H. (2010). Texture analysis with MTEX – Free and open source software toolbox. Diffusion and Defect Data–Solid State Data, Pt. B. *Solid State Phenomena*, *160*(February), 63–68. https://doi.org/10.4028/www.scientific.net/SSP.160.63

Baïsset, M., Labrousse, L., Schubnel, A., Gasc, J., Béneut, K., & Guillaumet, M. (2024). Rheology of hydrated plagioclase at lower crustal conditions: Cataclasis, creep and transformational plasticity. *Journal of Structural Geology*, *178*(105010), 105010. https://doi.org/10.1016/j.jsg.2023.105010

Baïsset, M., Yamato, P., & Duretz, T. (2024). Weakening induced by phase nucleation in metamorphic rocks: Insights from numerical models. *Geochemistry, Geophysics, Geosystems*, *25*(11), e2024GC011706. https://doi.org/10.1029/2024gc011706

Brune, J. N. (1970). Tectonic stress and the spectra of seismic shear waves from earthquakes. *Journal of Geophysical Research*, *75*(26), 4997–5009. https://doi.org/10.1029/JB075i026p04997

Burnley, P. C. (2005). Investigation of the martensitic-like transformation from Mg_2GeO_4 olivine to its spinel structure polymorph. *American Mineralogist*, *90*(8–9), 1315–1324. https://doi.org/10.2138/am.2005.1646

Burnley, P. C., Cline, C. J., & Drue, A. (2013). Kinking in Mg_2GeO_4 olivine: An EBSD study. *American Mineralogist*, *98*(5–6), 927–931. https://doi.org/10.2138/am.2013.4224

Burnley, P. C., Green, H. W., & Prior, D. J. (1991). Faulting associated with the olivine to spinel transformation in Mg_2GeO_4 and its implications for deep-focus earthquakes. *Journal of Geophysical Research*, *96*(B1), 425–443. https://doi.org/10.1029/90JB01937

Byerlee, J. D. (1968). Brittle-ductile transition in rocks. *Journal of Geophysical Research*, *73*(14), 4741–4750. https://doi.org/10.1029/JB073i014p04741

Byerlee, J. D. (1978). Friction of rocks. *Pure and Applied Geophysics*, *116*(4), 615–626. https://doi.org/10.1007/BF00876528

Cahn, J. W. (1956). The kinetics of grain boundary nucleated reactions. *Acta Metallurgica*, *4*(5), 449–459. https://doi.org/10.1016/0001-6160(56)90041-4

Cionoiu, S., Moulas, E., Stünitz, H., & Tajčmanová, L. (2022). Locally resolved stress-state in samples during experimental deformation: Insights into the effect of stress on mineral reactions. *Journal of Geophysical Research: Solid Earth*, *127*(8), e2022JB024814. https://doi.org/10.1029/2022JB024814

Cionoiu, S., Moulas, E., & Tajčmanová, L. (2019). Impact of interseismic deformation on phase transformations and rock properties in subduction zones. *Scientific Reports*, *9*(1), 1–6. https://doi.org/10.1038/s41598-019-56130-6

Collins, D. S., & Paul Young, R. (2000). Lithological controls on seismicity in granitic rocks. *Bulletin of the Seismological Society of America*, *90*(3), 709–723. https://doi.org/10.1785/0119990142

Dachille, F., & Roy, R. (1960). High pressure studies of the system Mg_2GeO_4-Mg_2SiO_4 with special reference to the olivine-spinel transition. *American Journal of Science*, *258*(4), 225–246. https://doi.org/10.2475/ajs.258.4.225

Domański, B., & Gibowicz, S. J. (2008). Comparison of source parameters estimated in the frequency and time domains for seismic events at the rudna copper mine, Poland. *Acta Geophysica*, *56*(2), 324–343. https://doi.org/10.2478/s11600-008-0014-1

Eshelby, J. D. (1957). The determination of the elastic field of an ellipsoidal inclusion, and related problems. *Proceedings of the Royal Society of London. Series A, Mathematical and Physical Sciences*, *241*(1226), 376–396. https://doi.org/10.1098/rspa.1957.0133

Frohlich, C. (1989). The nature of deep-focus earthquakes. *Annual Review of Earth and Planetary Sciences*, *17*(1), 227–254. https://doi.org/10.1146/annurev.ea.17.050189.001303

Frohlich, C. (2006). *Deep earthquakes*. Cambridge University Press.

Fukao, Y., & Kikuchi, M. (1987). Source retrieval for mantle earthquakes by iterative deconvolution of long-period P-waves. *Tectonophysics*, *144*(1), 249–269. https://doi.org/10.1016/0040-1951(87)90021-7

Fukuda, J.-I., Muto, J., & Nagahama, H. (2018). Strain localization and fabric development in polycrystalline anorthite + melt by water diffusion in an axial deformation experiment. *Earth Planets and Space*, *70*(1), 3. https://doi.org/10.1186/s40623-017-0776-2

Gasc, J., Daigre, C., Moarefvand, A., Deldicque, D., Fauconnier, J., Gardonio, B., et al. (2022). Deep-focus earthquakes: From high-temperature experiments to cold slabs. *Geology*, *50*(9), 1018–1022. https://doi.org/10.1130/g50084.1

Gasc, J., Gardonio, B., Deldicque, D., Daigre, C., Moarefvand, A., Petit, L., et al. (2022). Ductile vs. brittle strain localization induced by the Olivine–Ringwoodite transformation. *Minerals*, *12*(6), 719. https://doi.org/10.3390/min12060719

Gerya, T. V., Bercovici, D., & Becker, T. W. (2021). Dynamic slab segmentation due to brittle–ductile damage in the outer rise. *Nature*, *599*(7884), 245–250. https://doi.org/10.1038/s41586-021-03937-x

Green, H. W., & Burnley, P. C. (1989). A new self-organizing mechanism for deep-focus earthquakes. *Nature*, *341*(6244), 733–737. https://doi.org/10.1038/341733a0

Green, H. W., & Houston, H. (1995). The mechanics of deep earthquakes. *Annual Review of Earth and Planetary Sciences*, *23*(1), 169–213. https://doi.org/10.1146/annurev.ea.23.050195.001125

Green, H. W., Scholz, C. H., Tingle, T. N., Young, T. E., & Koczynski, T. A. (1992). Acoustic emissions produced by anticrack faulting during the olivine→spinel transformation. *Geophysical Research Letters*, *19*(8), 789–792. https://doi.org/10.1029/92GL00751

Guest, A., Schubert, G., & Gable, C. W. (2003). Stress field in the subducting lithosphere and comparison with deep earthquakes in Tonga. *Journal of Geophysical Research*, *108*(B6), 1–16. https://doi.org/10.1029/2002jb002161

Guest, A., Schubert, G., & Gable, C. W. (2004). Stresses along the metastable wedge of olivine in a subducting slab: Possible explanation for the Tonga double seismic layer. *Physics of the Earth and Planetary Interiors*, *141*(4), 253–267. https://doi.org/10.1016/j.pepi.2003.11.012

Gutenberg, B., & Richter, C. F. (1939). Depth and geographical distribution of deep-focus earthquakes: Second paper. *Bulletin of the Geological Society of America*, *50*(10), 1511–1528. https://doi.org/10.1130/GSAB-50-1511

Hacker, B. R., Abers, G. A., & Peacock, S. M. (2003). Subduction factory 1. theoretical mineralogy, densities, seismic wave speeds, and H_2O contents. *Journal of Geophysical Research*, *108*(B1), 1–26. https://doi.org/10.1029/2001jb001127

Hacker, B. R., Peacock, S. M., Abers, G. A., & Holloway, S. D. (2003). Subduction factory 2. are intermediate-depth earthquakes in subducting slabs linked to metamorphic dehydration reactions? *Journal of Geophysical Research*, *108*(B1). https://doi.org/10.1029/2001jb001129

Hanks, T. C., & Kanamori, H. (1979). A moment magnitude scale. *Journal of Geophysical Research*, *84*(B5), 2348–2350. https://doi.org/10.1029/JB084iB05p02348

Hielscher, R., & Schaeben, H. (2008). A novel pole figure inversion method: Specification of the MTEX algorithm. *Journal of Applied Crystallography*, *41*(6), 1024–1037. https://doi.org/10.1107/S0021889808030112

Hirth, G., & Tullis, J. (1992). Dislocation creep regimes in quartz aggregates. *Journal of Structural Geology*, *14*(2), 145–159. https://doi.org/10.1016/0191-8141(92)90053-Y

Hobbs, B. E., & Ord, A. (1988). Plastic instabilities: Implications for the origin of intermediate and deep focus earthquakes. *Journal of Geophysical Research*, *93*(B9), 10521–10540. https://doi.org/10.1029/jb093ib09p10521

Holyoke, C. W., & Kronenberg, A. K. (2010). Accurate differential stress measurement using the molten salt cell and solid salt assemblies in the griggs apparatus with applications to strength, piezometers and rheology. *Tectonophysics*, *494*(1–2), 17–31. https://doi.org/10.1016/j.tecto.2010.08.001

Holyoke, C. W., & Tullis, J. (2006). Mechanisms of weak phase interconnection and the effects of phase strength contrast on fabric development. *Journal of Structural Geology*, *28*(4), 621–640. https://doi.org/10.1016/j.jsg.2006.01.008

Ide, S., Beroza, G. C., Prejean, S. G., & Ellsworth, W. L. (2003). Apparent break in earthquake scaling due to path and site effects on deep borehole recordings. *Journal of Geophysical Research*, *108*(B5), 2271. https://doi.org/10.1029/2001jb001617

Incel, S., Hilairet, N., Labrousse, L., John, T., Deldicque, D., Ferrand, T., et al. (2017). Laboratory earthquakes triggered during eclogitization of lawsonite-bearing blueschist. *Earth and Planetary Science Letters*, *459*(December), 320–331. https://doi.org/10.1016/j.epsl.2016.11.047

Jia, Z., Fan, W., Mao, W., Shearer, P. M., & May, D. A. (2025). Dual mechanism transition controls rupture development of large deep earthquakes. *AGU advances*, *6*(3), e2025AV001701. https://doi.org/10.1029/2025av001701

Jiao, W., Silver, P. G., Fei, Y., & Prewitt, C. T. (2000). Do intermediate- and deep-focus earthquakes occur on preexisting weak zones? An examination of the Tonga subduction zone. *Journal of Geophysical Research*, *105*(B12), 28125–28138. https://doi.org/10.1029/2000jb900314

John, T., Medvedev, S., Rüpke, L. H., Andersen, T. B., Podladchikov, Y. Y., & Austrheim, H. (2009). Generation of intermediate-depth earthquakes by self-localizing thermal runaway. *Nature Geoscience*, *2*(2), 137–140. https://doi.org/10.1038/ngeo419

Kanamori, H., & Anderson, D. L. (1975). Theoretical basis of some empirical relations in seismology. *Bulletin of the Seismological Society of America*, *65*(5), 1073–1095. https://doi.org/10.1785/BSSA0650051073

Kanamori, H., Anderson, D. L., & Heaton, T. H. (1998). Frictional melting during the rupture of the 1994 Bolivian earthquake. *Science*, *279*(5352), 839–842. https://doi.org/10.1126/science.279.5352.839

Karato, S.-I., Riedel, M. R., & Yuen, D. A. (2001). Rheological structure and deformation of subducted slabs in the mantle transition zone: Implications for mantle circulation and deep earthquakes. *Physics of the Earth and Planetary Interiors*, *127*(1–4), 83–108. https://doi.org/10.1016/S0031-9201(01)00223-0

Kawakatsu, H., & Yoshioka, S. (2011). Metastable olivine wedge and deep dry cold slab beneath southwest Japan. *Earth and Planetary Science Letters*, *303*(1–2), 1–10. https://doi.org/10.1016/j.epsl.2011.01.008

Kerschhofer, L., Sharp, T. G., & Rubie, D. C. (1996). Intracrystalline transformation of olivine to wadsleyite and ringwoodite under subduction zone conditions. *Science*, *274*(5284), 79–81. https://doi.org/10.1126/science.274.5284.79

Kido, M., Muto, J., & Nagahama, H. (2016). Method for correction of differential stress calculations from experiments using the solid salt assembly in a griggs-type deformation apparatus. *Tectonophysics*, *672–673*, 170–176. https://doi.org/10.1016/j.tecto.2016.02.011

Kikuchi, M., & Kanamori, H. (1994). The mechanism of the deep Bolivia earthquake of June 9, 1994. *Geophysical Research Letters*, *21*(22), 2341–2344. https://doi.org/10.1029/94GL02483

Kirby, S. (1995). Interslab earthquakes and phase changes in subducting lithosphere. *Reviews of Geophysics*, *33*(1S), 287–297. https://doi.org/10.1029/95RG00353

Kirby, S., & Kronenberg, A. K. (1984). Deformation of clinopyroxenite: Evidence for a transition in flow mechanisms and semibrittle behavior. *Journal of Geophysical Research*, *89*(B5), 3177–3192. https://doi.org/10.1029/jb089ib05p03177

Kohlstedt, D. L., Evans, B., & others (1995). Strength of the lithosphere: Constraints imposed by laboratory experiments. *Journal of Geophysical Research*, *100*(B9), 17587–17602. https://doi.org/10.1029/95JB01460

Korenaga, J. (2007). Thermal cracking and the deep hydration of oceanic lithosphere: A key to the generation of plate tectonics? *Journal of Geophysical Research*, *112*(B5), 1–20. https://doi.org/10.1029/2006jb004502

Kubo, T., Ohtani, E., & Funakoshi, K.-I. (2004). Nucleation and growth kinetics of the α-β transformation in Mg_2SiO_4 determined by in situ synchrotron powder X-ray diffraction. *American Mineralogist*, *89*, 285–293. https://doi.org/10.2138/am-2004-2-305

Kubo, T., Ohtani, E., Kato, T., Shinmei, T., & Fujino, K. (1998). Experimental investigation of the alpha-beta transformation of san carlos olivine single crystal. *Physics and Chemistry of Minerals*, *26*(1), 1–6. https://doi.org/10.1007/s002690050155

Liebermann, R. C. (1975). Elasticity of olivine (α), beta (β), and spinel (γ) polymorphs of germanates and silicates. *Geophysical Journal of the Royal Astronomical Society*, *42*(3), 899–929. https://doi.org/10.1111/j.1365-246X.1975.tb06458.x

Liu, M., Huang, Y., & Ritsema, J. (2020). Stress drop variation of deep-focus earthquakes based on empirical green's functions. *Geophysical Research Letters*, *47*(9), e2019GL086055. https://doi.org/10.1029/2019gl086055

Liu, M., Kerschhofer, L., Mosenfelder, J. L., & Rubie, D. C. (1998). The effect of strain energy on growth rates during the olivine-spinel transformation and implications for olivine metastability in subducting slabs. *Journal of Geophysical Research*, *103*(B10), 23897–23909. https://doi.org/10.1029/98jb00794

Madariaga, R. (1976). Dynamics of an expanding circular fault. *Bulletin of the Seismological Society of America*, *66*(3), 639–666. https://doi.org/10.1785/BSSA0660030639

Marty, S., Schubnel, A., Bhat, H. S., Aubry, J., Fukuyama, E., Latour, S., et al. (2023). Nucleation of laboratory earthquakes: Quantitative analysis and scalings. *Journal of Geophysical Research: Solid Earth*, *128*(3), e2022JB026294. https://doi.org/10.1029/2022jb026294

Moarefvand, A., Gasc, J., Fauconnier, J., Baïsset, M., Burdette, E., Labrousse, L., & Schubnel, A. (2021). A new generation griggs apparatus with active acoustic monitoring. *Tectonophysics*, *816*(April), 229032. https://doi.org/10.1016/j.tecto.2021.229032

Mogi, K. (1962). Study of elastic shocks caused by the fracture of heterogeneous materials and its relations to earthquake phenomena (Vol. *40*).

Negredo, A. M., Valera, J. L., & Carminati, E. (2004). Temspol: A MATLAB thermal model for deep subduction zones including major phase transformations. *Computers & Geosciences*, *30*(3), 249–258. https://doi.org/10.1016/j.cageo.2004.01.002

Ogawa, M. (1987). Shear instability in a viscoelastic material as the cause of deep focus earthquakes. *Journal of Geophysical Research*, *92*(B13), 13801–13810. https://doi.org/10.1029/jb092ib13p13801

Ohuchi, T., Higo, Y., Tange, Y., Sakai, T., Matsuda, K., & Irifune, T. (2022). In situ X-ray and acoustic observations of deep seismic faulting upon phase transitions in olivine. *Nature Communications*, *13*(1), 5213. https://doi.org/10.1038/s41467-022-32923-8

Omori, S., Komabayashi, T., & Maruyama, S. (2004). Dehydration and earthquakes in the subducting slab: Empirical link in intermediate and deep seismic zones. *Physics of the Earth and Planetary Interiors*, *146*(1–2), 297–311. https://doi.org/10.1016/j.pepi.2003.08.014

Post, A. D., Tullis, J., & Yund, R. A. (1996). Effects of chemical environment on dislocation creep of quartzite. *Journal of Geophysical Research*, *101*(B10), 22143–22155. https://doi.org/10.1029/96jb01926

Proctor, B., & Hirth, G. (2016). "ductile to brittle" transition in thermally stable antigorite gouge at mantle pressures. *Journal of Geophysical Research: Solid Earth*, *121*(3), 1652–1663. https://doi.org/10.1002/2015jb012710

Raleigh, C. B., & Paterson, M. S. (1965). Experimental deformation of serpentinite and its tectonic implications. *Journal of Geophysical Research*, *70*(16), 3965–3985. https://doi.org/10.1029/JZ070i016p03965

Riggs, E. M., & Green, H. W. II. (2005). A new class of microstructures which lead to transformation-induced faulting in magnesium germanate. *Journal of Geophysical Research*, *110*(B3), 1–15. https://doi.org/10.1029/2004jb003391

Ross, N. L., & Navrotsky, A. (1987). The Mg_2GeO_4 olivine-spinel phase transition. *Physics and Chemistry of Minerals*, *14*(5), 473–481. https://doi.org/10.1007/BF00628825

Sawa, S., Gasc, J., Miyajima, N., Schubnel, A., Baisset, M., & Muto, J. (2025). Dataset for magnitude distribution during phase transformation faulting: Implications for deep-focus earthquakes [Dataset]. *Mendeley Data*. https://doi.org/10.17632/ktywz92vtr.2

Sawa, S., Miyajima, N., Muto, J., & Nagahama, H. (2021). Strain-induced partial serpentinization of germanate olivine with a small amount of water. *American Mineralogist*, *106*(11), 1789–1796. https://doi.org/10.2138/am-2021-7735

Sawa, S., Muto, J., & Nagahama, H. (2023). Modeling of olivine-spinel phase transformation of germanate olivine (Mg_2GeO_4) by using the phase-field method. *Physics of the Earth and Planetary Interiors*, *341*, 107060. https://doi.org/10.1016/j.pepi.2023.107060

Schmeling, H., Monz, R., & Rubie, D. C. (1999). The influence of olivine metastability on the dynamics of subduction. *Earth and Planetary Science Letters*, *165*(1), 55–66. https://doi.org/10.1016/S0012-821X(98)00249-0

Scholz, C. H. (1988). The brittle-plastic transition and the depth of seismic faulting. *Geologische Rundschau: Zeitschrift fur allgemeine Geologie*, *77*(1), 319–328. https://doi.org/10.1007/BF01848693

Scholz, C. H. (1998). Earthquakes and friction laws. *Nature*, *391*(6662), 37–42. https://doi.org/10.1038/34097

Schubnel, A., Brunet, F., Hilairet, N., Gasc, J., Wang, Y., & Green, H. W. (2013). Deep-focus earthquake analogs recorded at high pressure and temperature in the laboratory. *Science*, *341*(6152), 1377–1380. https://doi.org/10.1126/science.1240206

Shi, F., Zhang, J., Xia, G., Jin, Z., & Green, H. W. (2015). Rheology of Mg_2GeO_4 olivine and spinel harzburgite: Implications for earth's mantle transition zone. *Geophysical Research Letters*, *42*(7), 2212–2218. https://doi.org/10.1002/2015GL063316

Shiraishi, R., Muto, J., Tsunoda, A., Sawa, S., & Suzuki, J. (2022). Localized deformation of lawsonite during cold subduction. *Journal of Geophysical Research: Solid Earth*, *127*(2), e2021JB022134. https://doi.org/10.1029/2021jb022134

Sibson, R. H. (1982). Fault zone models, heat flow, and the depth distribution of earthquakes in the continental crust of the United States. *Bulletin of the Seismological Society of America*, *72*(1), 151–163. https://doi.org/10.1785/BSSA0720010151

Silver, P. G., Beck, S. L., Wallace, T. C., Meade, C., Myers, S. C., James, D. E., & Kuehnel, R. (1995). Rupture characteristics of the deep bolivian earthquake of 9 June 1994 and the mechanism of deep-focus earthquakes. *Science*, *268*(5207), 69–73. https://doi.org/10.1126/science.268.5207.69

Simpson, C. (1985). Deformation of granitic rocks across the brittle-ductile transition. *Journal of Structural Geology*, *7*(5), 503–511. https://doi.org/10.1016/0191-8141(85)90023-9

Speciale, P. A., Behr, W. M., Hirth, G., & Tokle, L. (2020). Rates of olivine grain growth during dynamic recrystallization and postdeformation annealing. *Journal of Geophysical Research: Solid Earth*, *125*(11), e2020JB020415. https://doi.org/10.1029/2020jb020415

Suzuki, M., & Yagi, Y. (2011). Depth dependence of rupture velocity in deep earthquakes. *Geophysical Research Letters*, *38*(5), 1–5. https://doi.org/10.1029/2011GL046807

Tibi, R., Bock, G., & Wiens, D. A. (2003). Source characteristics of large deep earthquakes: Constraint on the faulting mechanism at great depths. *Journal of Geophysical Research*, *108*(B2), 1–25. https://doi.org/10.1029/2002jb001948

Tingle, T. N., Green, H. W., Young, T. E., & Koczynski, T. A. (1993). Improvements to griggs-type apparatus for mechanical testing at high pressures and temperatures. *Pure and Applied Geophysics*, *141*(2–4), 523–543. https://doi.org/10.1007/BF00998344

Utsu, T. (1974). A three-parameter formula for magnetude distribution of earthquakes. *Journal of Physics of the Earth*, *22*(1), 71–85. https://doi.org/10.4294/jpe1952.22.71

Vaughan, P. J., & Coe, R. S. (1981). Creep mechanism in Mg_2GeO_4: Effects of a phase transition. *Journal of Geophysical Research*, *86*(B1), 389–404. https://doi.org/10.1029/JB086iB01p00389

Wadati, K. (1928). Unusual nature of deep-sea earthquakes—On the three types of earthquakes. *Kishoshushi*, *6*, 1–43.

Wang, J., Zhao, D., & Yao, Z. (2017). Seismic anisotropy evidence for dehydration embrittlement triggering intermediate-depth earthquakes. *Scientific Reports*, *7*(1), 1–9. https://doi.org/10.1038/s41598-017-02563-w

Wiens, D. A. (2001). Seismological constraints on the mechanism of deep earthquakes: Temperature dependence of deep earthquake source properties. *Physics of the Earth and Planetary Interiors*, *127*(1–4), 145–163. https://doi.org/10.1016/S0031-9201(01)00225-4

Wiens, D. A., & McGuire, J. J. (1995). The 1994 Bolivia and Tonga events: Fundamentally different types of deep earthquakes? *Geophysical Research Letters*, *22*(16), 2245–2248. https://doi.org/10.1029/95GL01598

Wiens, D. A., McGuire, J. J., & Shore, P. J. (1993). Evidence for transformational faulting from a deep double seismic zone in Tonga. *Nature*, *364*(6440), 790–793. https://doi.org/10.1038/364790a0

Wu, Q., & Chapman, M. (2017). Stress-Drop estimates and source scaling of the 2011 mineral, Virginia, mainshock and aftershocks. *Bulletin of the Seismological Society of America*, *107*(6), 2703–2720. https://doi.org/10.1785/0120170098

Wyss, M., & Molnar, P. (1972). Source parameters of intermediate and deep focus earthquakes in the Tonga arc. *Physics of the Earth and Planetary Interiors*, *6*(4), 279–292. https://doi.org/10.1016/0031-9201(72)90011-8

Yamada, T., Mori, J. J., Ide, S., Abercrombie, R. E., Kawakata, H., Nakatani, M., et al. (2007). Stress drops and radiated seismic energies of microearthquakes in a south african gold mine. *Journal of Geophysical Research*, *112*(B3). https://doi.org/10.1029/2006jb004553

Yoshimitsu, N., Kawakata, H., & Takahashi, N. (2014). Magnitude -7 level earthquakes: A new lower limit of self-similarity in seismic scaling relationships. *Geophysical Research Letters*, *41*(13), 4495–4502. https://doi.org/10.1002/2014GL060306

Zhan, Z. (2017). Gutenberg–richter law for deep earthquakes revisited: A dual-mechanism hypothesis. *Earth and Planetary Science Letters*, *461*, 1–7. https://doi.org/10.1016/j.epsl.2016.12.030

Zhan, Z. (2020). Mechanisms and implications of deep earthquakes. *Annual Review of Earth and Planetary Sciences*, *48*(1), 1–28. https://doi.org/10.1146/annurev-earth-053018-060314

Zhan, Z., Kanamori, H., Tsai, V. C., Helmberger, D. V., & Wei, S. (2014). Rupture complexity of the 1994 Bolivia and 2013 sea of okhotsk deep earthquakes. *Earth and Planetary Science Letters*, *385*, 89–96. https://doi.org/10.1016/j.epsl.2013.10.028

Zhang, H., van der Lee, S., Bina, C. R., & Ge, Z. (2021). Deep dehydration as a plausible mechanism of the 2013 mw 8.3 sea of okhotsk deep-focus earthquake. *Frontiers of Earth Science in China*, *9*(August), 1–13. https://doi.org/10.3389/feart.2021.521220

References From the Supporting Information

Beck, A. E., Darbha, D. M., & Schloessin, H. H. (1978). Lattice conductivities of single-crystal and polycrystalline materials at mantle pressures and temperatures. *Physics of the Earth and Planetary Interiors*, *17*(1), 35–53. https://doi.org/10.1016/0031-9201(78)90008-0

Roy, D. M., & Roy, R. (1954). An experimental study of the formation and properties of synthetic serpentines and related layer silicate minerals. *American Mineralogist*, *39*(53), 957–975.